Jagiellonian University
Faculty of Physics, Astronomy and Applied Computer Science

Daria Kisielewska

Studies of CPT symmetry violation in matter-antimatter systems

Doctoral thesis

Supervised by
prof. dr hab. Paweł Moskal
and
dr Eryk Czerwiński

Cracow 2018

DECLARATION

Wydział Fizyki, Astronomii i Informatyki Stosowanej
Uniwersytet Jagielloński

Oświadczenie

Ja niżej podpisana Daria Kisielewska (z domu Kamińska) (nr indeksu: 1055739) doktorantka Wydziału Fizyki, Astronomii i Informatyki Stosowanej Uniwersytetu Jagiellońskiego oświadczam, że przedłożona przeze mnie rozprawa doktorska pt. *Studies of CPT symmetry violation in matter-antimatter systems* jest oryginalna i przedstawia wyniki badań wykonanych przeze mnie osobiście, pod kierunkiem prof. dr hab. Pawła Moskala i dr Eryka Czerwińskiego. Pracę napisałam samodzielnie.

Oświadczam, że moja rozprawa doktorska została opracowana zgodnie z Ustawą o prawie autorskim i prawach pokrewnych z dnia 4 lutego 1994 r. (Dziennik Ustaw 1994 nr 24 poz. 83 wraz z późniejszymi zmianami). Jestem świadoma, że niezgodność niniejszego oświadczenia z prawdą ujawniona w dowolnym czasie, niezależnie od skutków prawnych wynikających z ww. ustawy, może spowodować unieważnienie stopnia nabytego na podstawie tej rozprawy.

Kraków, dnia ______________ ______________________________

Daria Kisielewska

I believe in evidence. I believe in observation, measurement, and reasoning, confirmed by independent observers. I'll believe anything, no matter how wild and ridiculous, if there is evidence for it. The wilder and more ridiculous something is, however, the firmer and more solid the evidence will have to be.

— Isaac Asimov, The Roving Mind

This thesis is dedicated to my boys.

ABSTRACT

In this thesis systems made of quark-antiquark and lepton-antilepton were studied for $\mathcal{CPT}$ symmetry violation effects.

The first study was preformed in neutral K meson pairs by comparing the asymmetries constructed from the decay rates into the two $\mathcal{CP}$ conjugated semileptonic final states, $\pi^- e^+ \nu$ and $\pi^+ e^- \bar{\nu}$. If the $\mathcal{CPT}$ symmetry holds, then the asymmetry constructed for short-lived kaon (A_S) and long-lived kaon (A_L) are expected to be identical. At present, the most precise measurement of A_L has been performed by the KTeV collaboration: $A_L = (3.322 \pm 0.058_{stat} \pm 0.047_{syst}) \times 10^{-3}$. The measurement of its counterpart is experimentally more difficult since it requires a very pure K_S beam which can be realised only by exploiting the entangled neutral kaons pairs produced at a ϕ-factory. The first measurement of A_S has been performed by the KLOE collaboration in 2006 using 410 pb^{-1} of integrated luminosity: $A_S = (1.5 \pm 9.6_{stat} \pm 2.9_{syst}) \times 10^{-3}$, with an accuracy dominated by the statistical uncertainty. The new measurement reported in this thesis is based on a four times larger data sample, corresponding to an integrated luminosity of 1.63 fb^{-1}. The final value $A_S = (-4.9 \pm 5.7_{stat} \pm 2.6_{syst}) \times 10^{-3}$ improves statistical accuracy by a factor of almost two with respect to the previous KLOE result. The combination of these two measurements gives $A_S = (-3.8 \pm 5.0_{stat} \pm 2.6_{syst}) \times 10^{-3}$ and allows to determine the new limits on $\mathcal{CPT}$ violating parameters $Re(x_-) = (-2.0 \pm 1.4) \times 10^{-3}$, and $Re(y) = (1.7 \pm 1.4) \times 10^{-3}$. The obtained results are in agreement with $\mathcal{CPT}$ invariance and with statistical uncertainty almost a factor of two smaller with respect to the former measurements.

The second part of this work comprised a demonstration of the feasibility of using the J-PET detector to test the $\mathcal{CPT}$ violation in correlations of momenta of photons originating from ortho-positronium annihilation and the spin of ortho-positronium. For this purpose simulations of the o-Ps formation and its annihilation into three photons were performed taking into account distributions of photons' momenta as predicted by quantum electrodynamics and the response of the J-PET tomograph. The results indicate that the J-PET detector has a realistic chance to improve best present limits established for $\mathcal{CPT}$ symmetry violations in decays of positronium by more than an order of magnitude. This can be achieved by the application of plastic scintillators which have superior time resolution and allow to create a setup with high granularity of detection strips and low detection pile-ups, which allows to overcome the limitation on the source activity. In addition, the improved angular resolution combined with the excellent timing, and with the possibility of triggerless registration of all events allow for suppression and monitoring of background events.

STRESZCZENIE

W prezentowanej pracy przedstawione są wyniki badań stopnia łamania symetrii $\mathcal{CPT}$ w systemach kwark-antykwark oraz lepton-antylepton.

Prowadzone pomiary polegają na porównaniu asymetrii ładunkowej w rozpadach półleptonowych $\pi^- e^+ \nu$ i $\pi^+ e^- \bar{\nu}$ neutralnych mezonów K. Jeśli symetria $\mathcal{CPT}$ jest zachowana w tym procesie, to asymetria ładunkowa wyznaczona dla kaonu krótko-życiowego (A_S) ma wartość równą asymetrii ładunkowej kaonu długo-życiowego (A_L). Dotychczas najdokładniejszy pomiar A_L uzyskany został w eksperymencie KTeV: $A_L = (3.322 \pm 0.058_{stat} \pm 0.047_{syst}) \times 10^{-3}$. Pomiar A_S przeprowadzony został przez zespół KLOE: $A_S = (1.5 \pm 9.6_{stat} \pm 2.9_{syst}) \times 10^{-3}$ przy użyciu 410 pb^{-1} danych. Uzyskany wynik zdominowany jest przez niepewność statystyczną. Niniejsza praca prezentuje analizę 1.63 fb^{-1} danych zebranych detektorem KLOE w latach 2004-2005. Otrzymana wartość wynosi: $A_S = (-4.9 \pm 5.7_{stat} \pm 2.6_{syst}) \times 10^{-3}$ i w połączeniu z poprzednim pomiarem pozwala na uzyskanie najbardziej precyzyjnej wartości tej wielkości na świecie: $A_S = (-3.8 \pm 5.0_{stat} \pm 2.6_{syst}) \times 10^{-3}$. Wyznaczone zostały także parametry opisujące stopień łamania symetrii $\mathcal{CPT}$: $Re(x_-) = (-2.0 \pm 1.4) \times 10^{-3}$, i $Re(y) = (1.7 \pm 1.4) \times 10^{-3}$. Uzyskane wyniki nie wskazują na łamanie symetrii $\mathcal{CPT}$.

Druga część pracy skupia się na wykazaniu możliwości użycia detektora J-PET do testu symetrii $\mathcal{CPT}$. Badaną obserwablą jest korelacja między wektorami pędu kwantów gamma pochodzących z anihilacji stanu orto-Pozytonium a wektorem spinu. W tym celu stworzone zostały kompleksowe symulacje komputerowe uwzględniające rozkłady pędów kwantów anihilacyjnych wynikające z przewidywań elektrodynamiki kwantowej oraz własności detektora J-PET. Otrzymane wyniki wskazują na możliwość polepszenia aktualnych parametrów opisujących łamanie symetrii $\mathcal{CPT}$ o rząd wielkości. Możliwe to będzie dzięki zastosowaniu w detektorze J-PET scyntylatorów plastikowych, które pozwolą na użycie źródła o wysokiej aktywności. Dodatkowymi atutami są: dobra rozdzielczość kątowa, wysoka dokładność pomiaru czasu oraz zapisywanie wszystkich zebranych zdarzeń, pozwalające na separację fotonów pochodzących z anihilacji stanu orto-Pozytonium i bezpośredniej anihilacji e^+e^- oraz monitorowanie tła.

ACKNOWLEDGMENTS

First of all, I would like to thank Dr. Eryk Czerwiński and Prof. Paweł Moskal without whose supervision this thesis would not exist. I owe an enormous gratitude to Eryk who has been there as my supervisor for the past years and has been relentless in his support and constructive critique. I am greatly indebted also to Prof. Moskal for giving me the opportunity to work within his research group and for his support and guidance during the preparation of this thesis.

I would also like to extend my appreciation to Prof. Antonio Di Domenico and Dr. Erika de Lucia for their constructive comments and careful supervision of my analysis.

Special thanks to Prof. Giogio Capon, Prof. Wojciech Wiślicki, Dr. Michał Silarski, Dr. Wojciech Krzemień, Dr. Antonio De Santis for their suggestions and remarks during our group meetings.

I also thank my Colleagues from Laboratories of Frascati: Dr. Elena Perez del Rio, Dr. Marcin Berłowski and Dr. Gianfranco Morello as well as from the J-PET experiment: Dr. Aleksander Gajos, Ewelina Kubicz, Monika Pawlik-Niedźwiecka, Szymon Niedźwiecki, Dominika Alfs, Krzysztof Kacprzak, Dr. Magdalena Skurzok, Dr. Grzegorz Korcyl and Dr. Sushil Sharma. I thank them for their companionship and for providing a pleasurable and friendly working atmosphere.

Finally, I wish to thank my family: Justyna, Andrzej and Konrad for their support and countless Skype connections. To Katarzyna and Michał for their assistance and patience throughout these years. To Kaja and Gapa for cycling trips and boardgame parties. To Danuta and Helena for visits and kindness.

Special thanks to Tomek, my best friend and husband, and the newest family additions: our two little boys, who have been kind enough to let me finish this thesis.

This work was supported by the Polish National Science Centre through the Grants Number 2014/14/E/ST2/00262, 2016/23/N/ST2/01293, 2016/21/B/ST2/01222, and by the Ministry of Science and Higher Education through the grant 7150/E-338/M/2017.

CONTENTS

1 DISCRETE SYMMETRIES IN PHYSICS

The idea of symmetry is widely used in modern physics, since a set of physical phenomena exhibits common symmetries. Symmetry arguments can be guiding principles to understand new phenomena and put limitations on considered theories.

According to the Noether's theorem, symmetries are associated with a transformation of a system and for every global continuous symmetry there exists an associated time independent quantity [1]. Thus the invariances of laws of physics under translations of time, space or rotation imply conservation of energy, momentum, or angular momentum, respectively. Discrete symmetries of nature such as charge conjugation ($\mathcal{C}$), parity inversion ($\mathcal{P}$) or time reversal ($\mathcal{T}$) do not lead to new conserved quantities. To the best of our knowledge, few symmetries are really exact in nature. The $\mathcal{C}$, $\mathcal{P}$ and $\mathcal{CP}$ are violated in the weak interactions. An example studied in this thesis is the $\mathcal{CPT}$ symmetry, which is strongly embedded into the theoretical framework of modern physics. This is expressed in the $\mathcal{CPT}$ theorem[1] that can be stated as follows [5]: *Any quantum theory, formulated on flat space time is symmetric under the combined action of $\mathcal{CPT}$ transformations, provided the theory respects (i) Locality, (ii) Unitarity (i.e. conservation of probability) and (iii) Lorentz invariance.*

The formulation of this theorem may raise doubts as to why one should consider testing the $\mathcal{CPT}$ invariance, particularly taking into account the fact that all our phenomenology to date has been based on quantum theories with built in $\mathcal{CPT}$ conservation. Speculations on $\mathcal{CPT}$ symmetry violation recently arose in discussions of possible:

- testing the fundamentals of today's physics. A theorem presented by Greenberg [6] shows that violation of $\mathcal{CPT}$ automatically indicates violation of the Lorentz symmetry. For this reason the studies of Lorentz invariance and $\mathcal{CPT}$ tests are strongly linked. Searches in a wide range of different systems are summarized in Reference [7].
- searching for physics beyond the Standard Model. The spontaneous Lorentz and $\mathcal{CPT}$ violation could occur in more extended models. For example the string structure of the universe may cause spontaneous $\mathcal{CPT}$ symmetry breaking [8, 9].
- looking for the sources of matter-antimatter imbalance. In principle this can be explained by the Sakharov conditions [10]. However, the amount of $\mathcal{CP}$ violation predicted by the Standard Model is not sufficient to generate the observed overabundance of matter. The $\mathcal{CPT}$ violation could create the mechanism in the early Universe that lead to the baryon asymmetry observed nowadays [11].

1 There exist several proofs of $\mathcal{CPT}$ theorem and they are based on slightly different initial general assumptions [2–4]. However, in most self-consistent theories the $\mathcal{CPT}$ theorem is automatically valid.

The size of possible $\mathcal{CPT}$ violation effects can be discussed only in the frame of an explicit fundamental theory. To date no evidence for $\mathcal{CPT}$ violation has been found, so any effects must be miniscule.

In this thesis two systems will be studied for possible $\mathcal{CPT}$ violation effects. The first one is the neutral kaon system. The performed test is based on comparison between semileptonic asymmetry in K_S decays:

$$A_S = \frac{\Gamma(K_S \to \pi^- e^+ \nu) - \Gamma(K_S \to \pi^+ e^- \bar{\nu})}{\Gamma(K_S \to \pi^- e^+ \nu) + \Gamma(K_S \to \pi^+ e^- \bar{\nu})}, \tag{1.1}$$

and its counterpart A_L [12] constructed for K_L. To date, the most precise measurement of A_L has been preformed by the KTeV collaboration: $A_L = (3.322 \pm 0.058_{stat} \pm 0.047_{syst}) \times 10^{-3}$ [13]. The precision achieved for A_L is two orders of magnitude better compared to the precision of $A_S = (1.5 \pm 9.6_{stat} \pm 2.9_{syst}) \times 10^{-3}$ determination [14]. The present accuracy of A_S determination is dominated by the statistical uncertainty. The measurement reported in this thesis is based on a four times larger data sample, corresponding to an integrated luminosity of 1.63 fb^{-1}, which allows to reach a twice smaller statistical error.

The second system is a purely leptonic electron-positron bound state called positronium. Its structure is analogous to the Bohr atom. The ortho-positronium triplet (o-Ps) and para-positronium singlet (p-Ps) states can be distinguished with different properties, determined by their spin. Due to the charge conjugation conservation the o-Ps can decay only into an odd number of photons, while the p-Ps into an even number, and the mean lifetime of o-Ps state in vacuum is longer (140 ns) than for p-Ps state (120 ps) [15]. Studies of discrete symmetries violation in an ortho-positronium state were proposed by Bernreuther et al. in 1988 [16]. The signals for discrete symmetries violation in a spin-polarized ortho-positronium will be visible in a selected set of angular correlations consisting of the i-th photon momentum $\vec{k}_i$ (photons are ordered by decreasing energy) and the ortho-positronium spin $\vec{s}$. The evidence for discrete symmetry violations could be observed in a non-vanishing value of one of the forbidden correlations, e.g. $\vec{s} \cdot \hat{k}_1 \times \hat{k}_2$ for $\mathcal{CPT}$ symmetry. Previous measurement of the $\mathcal{CPT}$ violation coefficient was conducted by Vetter and Freedman using the Gammasphere detector and resulted in violation amplitude parameters $C_{CPT} = 0.0026 \pm 0.0031$ consistent with zero [17]. In this thesis we will explore the possibility to study the $\mathcal{CPT}$ violation coefficient by the J-PET detector built at the Jagiellonian University.

The thesis consists of seven chapters. In the next chapter a brief introduction on phenomenology of semileptonic decays of neutral kaon and ortho-positronium annihilation is given. The next three chapters, comprising the first part, are dedicated to measurement of the charge asymmetry for the $K_S \to \pi e \nu$ decay and a test of $\mathcal{CPT}$ symmetry with the KLOE detector. The second chapter contains a description of the KLOE apparatus where the characteristics of the main sub-detectors are reported. The third chapter consists of data analysis description: an identification of K_S meson by its long-lived counterpart and criteria used to select $K_S \to \pi e \nu$ decays. The obtained value of A_S and determined $\mathcal{CPT}$ symmetry violation parameters are presented in the fourth chapter. The second part of the thesis consists of three chapters dedicated to the study of angular correlations in the positronium decay at the J-PET detector. Chapter five is devoted to a description of the J-PET detector made from plastics scintillators. A description of the preformed Monte Carlo simulation is given in chapter six, leading to conclusions and further plans summarized in the last chapter.

This thesis incorporates material from the following papers[2]:

- Measurement of the charge asymmetry for the $K_S \to \pi e \nu$ decay and test of CPT symmetry with the KLOE detector
  KLOE-2 Collaboration: A. Anastasi, (...), D. Kisielewska-Kamińska *et al.*
  JHEP 9 (2018) 21 [18]
- K_S semileptonic decays and test of CPT symmetry with the KLOE detector
  D. Kamińska for the KLOE-2 Collaboration
  Acta Phys. Polon. B46 (2015) 19 [19]
- A feasibility study of ortho-positronium decays measurement with the J-PET scanner based on plastic scintillators
  J-PET Collaboration: D. Kamińska *et al.*
  Eur. Phys. J. C76 (2016) 445 [20]
- Searches for discrete symmetries violation in ortho-positronium decay using the J-PET detector
  J-PET Collaboration: D. Kamińska *et al.*
  Nukleonika 60 (2015) 729 [21]

and conference reports [22–25].

The first part of the thesis uses materials from the short report of the $K_S \to \pi e \nu$ analysis status [19], and a final measurement of A_S value with the KLOE dataset [18]. The second part of the thesis is based on prospects of using the J-PET detector for ortho-positronium decays measurement [20] and discrete symmetries studies [21]. Some material from each of these papers has also been incorporated into this introductory chapter. In all cases the thesis author is the leading author of the papers and the main contributor to the conducted studies.

The developed Monte Carlo simulations, reported in the second part of the thesis, were used for exploring the possibility of three gamma photon imaging based on the ortho-positronium annihilation. These studies result in a patent [26] and additional article [27], not described in this dissertation.

1.1 NEUTRAL K MESONS SYSTEM

A neutral kaon system plays a special role in $\mathcal{CPT}$ violation searches. Due to its sensitivity to a variety of symmetry violation effects, it is one of the best candidates for such kind of studies. One of the possible tests is based on the comparison between semileptonic asymmetry in short-lived kaon meson (K_S) decays (A_S) and the analogous asymmetry in long-lived kaon meson (K_L) decays A_L [12]. To date,

2 Please note that the surname of the dissertation author 'Kamińska' was changed to 'Kisielewska' due to marriage.

the A_L [28] was determined with a precision more than two orders of magnitude better than A_S [14]:

$$A_L = (3.322 \pm 0.058_{stat} \pm 0.047_{syst}) \times 10^{-3}, \tag{1.2}$$
$$A_S = (1.5 \pm 9.6_{stat} \pm 2.9_{syst}) \times 10^{-3}. \tag{1.3}$$

The present accuracy of A_S determination is dominated by the statistical uncertainty. Therefore, the aim of this work was a determination of A_S with two times smaller statistical error due to four times bigger data sample and improved systematical uncertainties.

1.1.1 *Charge asymmetry in neutral kaon semileptonic decays*

Neutral kaons are the lightest particles which contain a strange quark. Observed K_S and K_L are linear combinations of flavour (strange) eigenstates (K^0 and $\bar{K^0}$):

$$\begin{aligned}
|K_S\rangle &= \frac{1}{\sqrt{2(1+|\epsilon_S|^2)}}\Big((1+\epsilon_S)\,|K^0\rangle + (1-\epsilon_S)\,|\bar{K^0}\rangle\Big)\,,\\
|K_L\rangle &= \frac{1}{\sqrt{2(1+|\epsilon_L|^2)}}\Big((1+\epsilon_L)\,|K^0\rangle - (1-\epsilon_L)\,|\bar{K^0}\rangle\Big)\,.
\end{aligned} \tag{1.4}$$

where the introduced small parameters ϵ_S and ϵ_L can be rewritten to separate $\mathcal{CP}$ and $\mathcal{CPT}$ violation parameters ϵ_K and δ_K, respectively:

$$\begin{aligned}
\epsilon_S &= \epsilon_K + \delta_K,\\
\epsilon_L &= \epsilon_K - \delta_K.
\end{aligned} \tag{1.5}$$

In the Standard Model a decay of K^0 (or $\bar{K^0}$) state is associated with the transition of the $\bar{s}$ quark into $\bar{u}$ quark (or s into u) and emission of the charged boson. Change of strangeness (ΔS) implies the corresponding change of electric charge (ΔQ) (see Figure 1.1). This effect is referred to as the $\Delta S = \Delta Q$ rule. Therefore, decays of $K^0 \to \pi^- e^+ \nu$ and $\bar{K^0} \to \pi^+ e^- \bar{\nu}$ are possible but $K^0 \to \pi^+ e^- \bar{\nu}$ and $\bar{K^0} \to \pi^- e^+ \nu$ are forbidden.

	initial state		**final state**
S	1	$\longrightarrow$	0
Q	0	$\longrightarrow$	1

	initial state		**final state**
S	-1	$\longrightarrow$	0
Q	0	$\longrightarrow$	-1

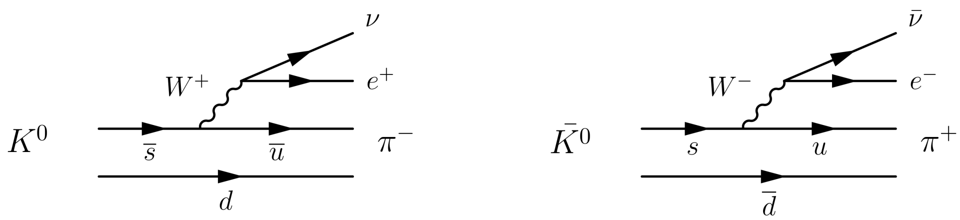

Figure 1.1: Feynman diagrams for K^0 and $\bar{K^0}$ semileptonic decay. Tables present the $\Delta S = \Delta Q$ rule.

Decay amplitudes for semileptonic decays of states $|K^0\rangle$ and $|\bar{K^0}\rangle$ can be written as follows [12]:

$$\begin{aligned} \langle \pi^- e^+ \nu | \, H_{weak} \, |K^0\rangle &= \mathcal{A}_+, \\ \langle \pi^+ e^- \bar{\nu} | \, H_{weak} \, |\bar{K^0}\rangle &= \bar{\mathcal{A}}_-, \\ \langle \pi^+ e^- \bar{\nu} | \, H_{weak} \, |K^0\rangle &= \mathcal{A}_-, \\ \langle \pi^- e^+ \nu | \, H_{weak} \, |\bar{K^0}\rangle &= \bar{\mathcal{A}}_+, \end{aligned} \tag{1.6}$$

where the H_{weak} is the term of Hamiltonian corresponding to the weak interaction and $\mathcal{A}_+, \bar{\mathcal{A}}_-, \mathcal{A}_-, \bar{\mathcal{A}}_+$ parametrize semileptonic decay amplitudes.

It is useful to introduce the following notation:

$$\begin{aligned} x &= \frac{\bar{\mathcal{A}}_+}{\mathcal{A}_+}, \\ \bar{x} &= \left(\frac{\mathcal{A}_-}{\bar{\mathcal{A}}_-}\right)^*, \\ y &= \frac{\bar{\mathcal{A}}_-^* - \mathcal{A}_+}{\bar{\mathcal{A}}_-^* + \mathcal{A}_+}, \\ x_\pm &= \frac{x \pm \bar{x}^*}{2} = \frac{1}{2}\left[\frac{\bar{\mathcal{A}}_+}{\mathcal{A}_+} \pm \left(\frac{\mathcal{A}_-}{\bar{\mathcal{A}}_-}\right)^*\right]. \end{aligned} \tag{1.7}$$

For further considerations, rules for applying symmetry operators to amplitudes of two spin zero systems A and B (and corresponding anti-systems $\overline{A}$ and $\overline{B}$) could be summarized as:

$$\begin{aligned} \langle \mathcal{T}\mathbf{B} | \, \mathcal{T} H_{weak} \mathcal{T}^{-1} \, |\mathcal{T}\mathbf{A}\rangle &= (\langle \mathbf{B} | \, \mathcal{T} H_{weak} \mathcal{T}^{-1} \, |\mathbf{A}\rangle)^* \\ \langle \mathcal{CP}\mathbf{B} | \, \mathcal{CP} H_{weak} \mathcal{CP}^{-1} \, |\mathcal{CP}\mathbf{A}\rangle &= \langle \overline{\mathbf{B}} | \, \mathcal{CP} H_{weak} \mathcal{CP}^{-1} \, |\overline{\mathbf{A}}\rangle \\ \langle \mathcal{CPT}\mathbf{B} | \, \mathcal{CPT} H_{weak} \mathcal{CPT}^{-1} \, |\mathcal{CPT}\mathbf{A}\rangle &= (\langle \overline{\mathbf{B}} | \, \mathcal{CPT} H_{weak} \mathcal{CPT}^{-1} \, |\overline{\mathbf{A}}\rangle)^*. \end{aligned} \tag{1.8}$$

One obtains the relation between the semileptonic amplitudes and conservation of a particular symmetry by applying the rules presented above to the states defined in Equation 1.6. These considerations are summarized in Table 1.1.

Table 1.1: Relations between discrete symmetries and semiletponic amplitudes

Conserved quantity	Required relation
$\Delta S = \Delta Q$ rule	$x = \bar{x} = 0$
$\mathcal{CPT}$ symmetry	$x = \bar{x}^*$, $y = 0$
$\mathcal{CP}$ symmetry	$x = \bar{x}$, $y = Im(y)$
$\mathcal{T}$ symmetry	$y = Re(y)$

The measured value of lepton charge asymmetry can be expressed in terms of x_-, x_+ and y:

$$\begin{aligned} A_S &= 2\left[Re\left(\epsilon_K\right) + Re\left(\delta_K\right) - Re(y) + Re(x_-)\right], \\ A_L &= 2\left[Re\left(\epsilon_K\right) - Re\left(\delta_K\right) - Re(y) - Re(x_-)\right]. \end{aligned} \tag{1.9}$$

From the sum and difference of A_S and A_L one can extract parameters accounting for possible violations of the $\mathcal{CPT}$ symmetry, either in the decay amplitudes (y) or in the mass matrix (δ_K):

$$(A_S - A_L)/4 = Re(\delta_K) + Re(x_-), \tag{1.10}$$
$$(A_S + A_L)/4 = Re(\epsilon_K) - Re(y). \tag{1.11}$$

The charge asymmetry for K_L decays was precisely determined by the KTeV experiment at Fermilab [28]. At present the most accurate measurement of K_S charge asymmetry was obtained by the KLOE collaboration [14]. The achieved charge asymmetry for K_S decays is consistent within error limits with charge asymmetry for K_L decays, which suggest conservation of $\mathcal{CPT}$ symmetry. However, this result is dominated by a statistical uncertainty which is three times larger than the systematic one, and it can be improved by analysing the 1.63 fb^{-1} total luminosity data sample acquired in 2004 and 2005 by the KLOE experiment.

1.2 POSITRONIUM ATOM

Interaction between electron-positron pair leads to direct annihilation into photons or creation of a bound state called positronium. This system decays through the annihilation of e^+ and e^- into photons depending on positronium's quantum mechanical state $\Phi_{n,l,m}(\vec{r})\,|S, S_z\rangle$, where the orbital wave function Φ is the hydrogen atom wave function with the electron mass replaced by the reduced mass of the electron-positron pair and where n, l, and m are the usual principle, orbital and magnetic quantum numbers, respectively. The spin is a linear combination of electron and positron spins, of which there are four possibilities:

$$\begin{aligned}
|S=1, S_z=1\rangle &= |\uparrow\rangle\,|\uparrow\rangle\,,\\
|S=1, S_z=0\rangle &= \frac{1}{\sqrt{2}}\left(|\uparrow\rangle\,|\downarrow\rangle + |\downarrow\rangle\,|\uparrow\rangle\right),\\
|S=1, S_z=-1\rangle &= |\downarrow\rangle\,|\downarrow\rangle\,,\\
|S=0, S_z=0\rangle &= \frac{1}{\sqrt{2}}\left(|\uparrow\rangle\,|\downarrow\rangle - |\downarrow\rangle\,|\uparrow\rangle\right),
\end{aligned} \tag{1.12}$$

where $|\uparrow\rangle$ and $|\downarrow\rangle$ denote $S_z = +\frac{1}{2}$ and $S_z = -\frac{1}{2}$ for a single electron (positron). The triplet state is called ortho-positronium, while anti-aligned singlet state is called para-positronium. Constrained by conservation laws, the ortho-positronium state can annihilate only to an odd number of photons, while the para-positronium state can decay only to an even number of photons. In practice, final states with larger photon numbers are suppressed by few orders of magnitude and the positronium annihilations are dominated by p-Ps$\rightarrow 2\gamma$ and o-Ps$\rightarrow 3\gamma$.

Positronium is a purely leptonic state which allows to determine its properties using quantum electrodynamics alone. The decay rates were found to be [29, 30]:

$$\begin{aligned}
\Gamma\,(\text{p-Ps} \rightarrow 2\gamma) &= \frac{1}{2}\frac{m_e c^2 \alpha^5}{\hbar} = 8.032 \times 10^{-9} s^{-1},\\
\Gamma\,(\text{o-Ps} \rightarrow 3\gamma) &= \frac{2(\pi^2-9)}{9\pi}\frac{m_e c^2 \alpha^6}{\hbar} = 7.211 \times 10^{-6} s^{-1},
\end{aligned} \tag{1.13}$$

where m_e is the mass of electron, c is the speed of light, α is the fine structure constant, and $\hbar$ is the reduced Planck constant. The additional power of α in Γ (o-Ps $\rightarrow 3\gamma$) follows directly from the Feynman rules given the additional photon in o-Ps decay. The inverse of the decay rates give the mean lifetimes of the states in vacuum [15]:

$$\begin{aligned} \tau_{o-Ps} &= 142 \text{ ns}, \\ \tau_{p-Ps} &= 0.125 \text{ ns}. \end{aligned} \tag{1.14}$$

1.2.1 *Positronium decay correlation test*

The positronium annihilation into photons can be used for tests of discrete symmetries invariance in the leptonic sector. Searches for those effects conducted to date, have taken three forms:

- looking for forbidden decays e.g. o-Ps$\rightarrow 2\gamma$ or o-Ps$\rightarrow 4\gamma$. The upper limit for those decays is in an order of 10^{-6} [31],
- studies of forbidden transitions in positronium energy spectrum [32],
- tests involving correlations of photons momenta originating form o-Ps annihilation.

In this thesis we will focus on the last listed test. The general theoretical framework for those studies has been shown in 1988 by Bernreuther *et al* [16], and has introduced the simplest correlation between the spin polarization vector $\vec{s}$ of o-Ps and a vector normal to the decay plane:

$$\vec{s} \cdot \left(\vec{k}_1 \times \vec{k}_2\right) \tag{1.15}$$

where $\vec{k}_1$ and $\vec{k}_2$ are the momenta of the two most energetic annihilation photons (see Figure 1.2). The $\mathcal{CPT}$ invariance implies vanishing of the aforementioned angular correlation.

A non-zero observed effect would be an evidence for a new interaction, and one needs to carefully investigate if this interaction violates $\mathcal{CPT}$ symmetry. The effects that may mimic the signal from $\mathcal{CPT}$ violation are following:

- the effects in final state interactions, originating from virtual creation of charged particle pairs. This effect is expected to be at the level of 10^{-9} [33],
- the weak interaction amplitudes, such as parity mixing and weak decays of positronium state. Those effects turn out to be at the level of 10^{-12} [16].

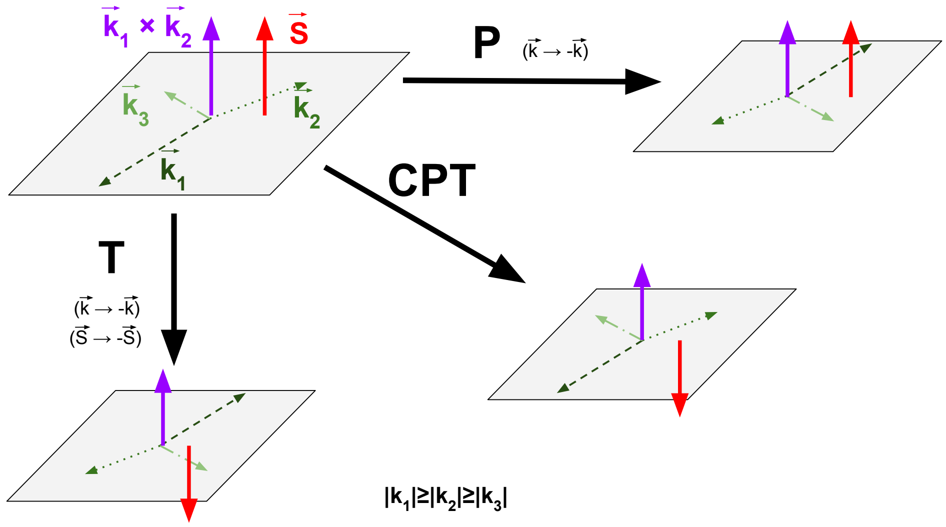

Figure 1.2: The vectors in an o-Ps→ 3γ event (in o-Ps frame of reference) used to construct operators used in searches for $\mathcal{CPT}$ symmetry violation. Momentum vectors are ordered by magnitude (green arrows; dashed, dotted, dashed-dotted). Vector product $\vec{k}_1 \times \vec{k}_2$ is a violet arrow, while the red arrow denotes the spin $\vec{S}$ of the decaying ortho-positronium. The top-left panel shows the reference state, while the others present the system after applying discrete symmetry operators: $\mathcal{T}$, $\mathcal{P}$ or $\mathcal{CPT}$.

Part I

MEASUREMENT OF THE CHARGE ASYMMETRY FOR THE $K_S \to \pi e \nu$ DECAY AND TEST OF CPT SYMMETRY WITH THE KLOE DETECTOR

2 THE KLOE EXPERIMENT

The KLOE detector operated at the DAΦNE electron-positron collider (see Figure 2.1) localized at National Laboratory in Frascati near Rome. The energy of two colliding beams is adjusted to produce the ϕ meson which decays predominantly into a pair of neutral or charged kaons. Main decay modes of the ϕ meson and neutral kaons are presented in Table 2.1. Since the beams cross at an angle of 2×12.5 mrad the ϕ-meson is produced with a small momentum of $p_\phi \approx 13$ MeV/c [34].

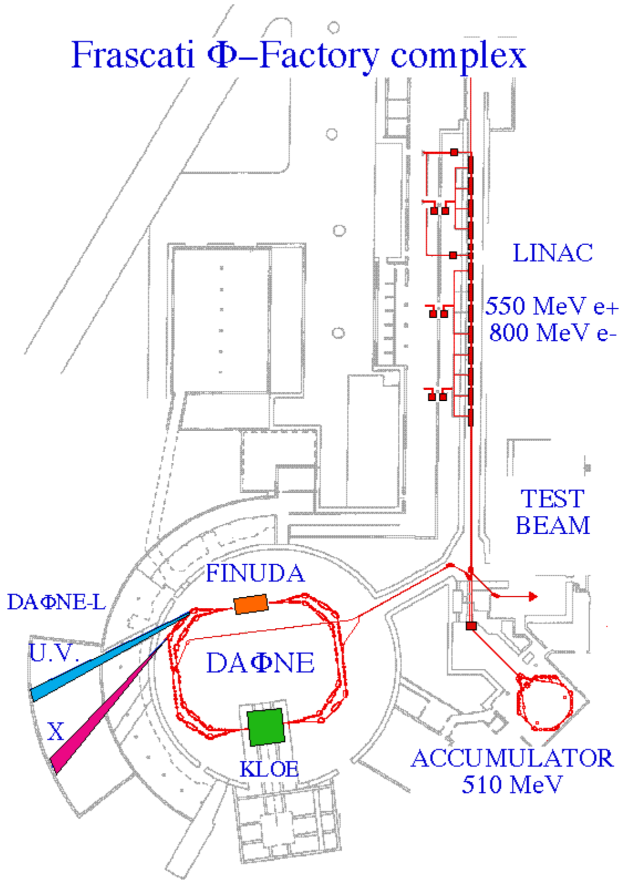

Figure 2.1: Schematic view of the DAΦNE accelerator complex. The positrons are created in an intermediate stage of the linear accelerator (LINIAC). Both electrons and positrons are accelerated in LINIAC, transfered to the accumulator ring and then injected into DAΦNE storage rings, at an energy of 510 MeV. The positrons and electron beams are circulating in separate rings with two intersection points. Figure adapted from Ref. [35].

The DAΦNE accelerator with average luminosity of 5×10^{32} cm^{-2}s^{-1} is capable of producing about 1300 kaon pairs per second. During two data taking campaigns,

Table 2.1: Main branching ratios of the ϕ meson and neutral kaons [36].

ϕ		K_S		K_L	
Channel	BR (%)	Channel	BR (%)	Channel	BR (%)
K^+K^-	48.9 ± 0.5	$\pi^+\pi^-$	69.30	$\pi^{\mp}e^{\pm}\nu$	40.55
K_SK_L	34.2 ± 0.4	$\pi^0\pi^0$	30.69	$\pi^{\mp}\mu^{\pm}\nu$	27.04
$\rho\pi$	15.32 ± 0.32	$\pi^{\mp}e^{\pm}\nu$	7.04×10^{-2}	$3\pi^0$	19.52
$\eta\gamma$	1.309 ± 0.024	$\pi^{\mp}\mu^{\pm}\nu$	4.69×10^{-2}	$\pi^+\pi^-\pi^0$	12.54

in 2001-2002 and 2004-2005, KLOE collected a data sample which corresponds to the integrated luminosity of 2.5 fb^{-1}.

The KLOE detector consists of two main components: the cylindrical drift chamber and the electromagnetic calorimeter, both surrounding the beam pipe. All elements are immersed in a 0.52 T magnetic field created by a superconducting coil placed along the beam axis. A schematic cross-section side view of the KLOE detector is shown in Figure 2.2.

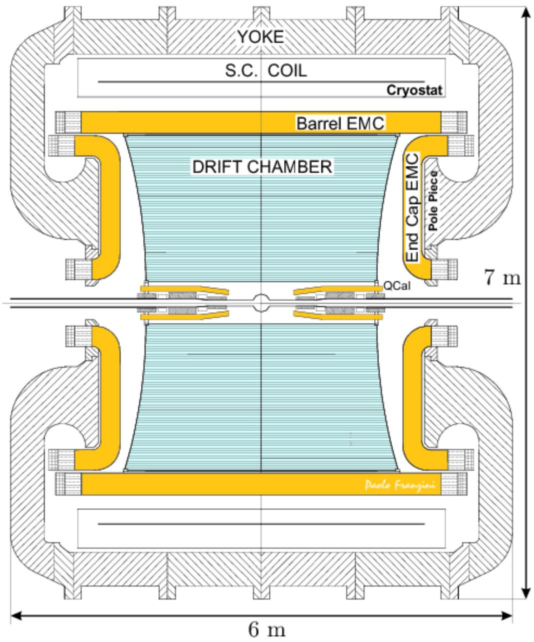

Figure 2.2: Vertical cross section of the KLOE detector along the beam line. The center part of the detector is an e^+e^- interaction point surrounded by the spherical beam pipe. Along the beam pipe the focusing quadrupoles are mounted instrumented with compact tile calorimeters (QCAL). The main components of the KLOE detector are a large drift chamber (DC), filled with a helium-based gas mixture, and an electromagnetic calorimeter (EMC) surrounding the DC. All detectors are immersed in a solenoidal magnetic field (0.52 T), to allow charged particle's momenta measurement. Figure adapted from Ref. [37].

2.1 DRIFT CHAMBER

The KLOE drift chamber (DC) [38] is a 3.3 m long cylinder with internal and external radii of 0.25 m and 2 m, respectively. The mechanical support of the DC consists mainly of two endplates and 12 external panels stretched between them. The gas sealing is provided by a 750 μm thick aluminated carbon fiber cylinder. A gas mixture composed of helium (90%) and isobutane (10%) acts as a quencher. These features maximize transparency to photons and reduce charged particle multiple scattering and $K_L \to K_S$ regeneration. About 40% of produced K_L mesons decay inside the DC volume, while most of the surviving K_L's interact and are detected in the electromagnetic calorimeter.

Between the DC endplates around 12500 sense wires are stretched creating cells, which are organized in coaxial layers with two different dimensions of a transverse plane: 2×2 cm^2 (12 inner layers) and 3×3 cm^2 (46 outer layers). In order to define the position along the z axis of the detector the neighbouring layers are twisted in the opposites directions by a small stereo angle [38].

The spacial resolution obtained in the r, φ plane is better than 200 μm, a resolution along the z axis of ~ 2 mm and the resolution of the decay vertex determination of ~ 1 mm. Moreover, the curvature of the reconstructed tracks allows to determine the particle momentum with a relative accuracy of 0.4 % [38].

The drift chamber allows to reconstruct the charged particle tracks and momenta while the calorimeter enables recording of time and energy of both charged and neutral particles.

2.2 ELECTROMAGNETIC CALORIMETER

The geometrical acceptance of the KLOE electromagnetic calorimeter (EMC) is almost 4π. The EMC consists of two main parts: 24 trapezoidal modules arranged into a barrel and 32 C-shaped modules that create the two endcaps closing the barrel. Each module consists of lead (48%), scintillating fibers (42%) and glue (10%). A schematic view is shown in Figure 2.3. For each module the readout is provided from both ends by photomultipliers connected to the module by the light guides.

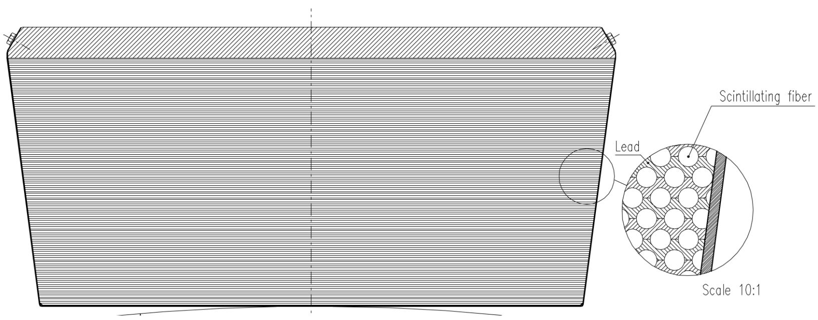

Figure 2.3: Schematic view of the fiber-lead composite of each module of the KLOE electromagnetic calorimeter. Figure adapted from Ref. [39].

The KLOE calorimeter has been designed to have an excellent accuracy of energy determination and time resolution: $\sigma(E)/E = 5.7\%/\sqrt{E[\text{GeV}]}$, $\sigma_t =$

$54\ \mathrm{ps}/\sqrt{E[\mathrm{GeV}]} \oplus 140\ \mathrm{ps}$ [40] in order to register the hits of neutral particles and provide a possibility of the Time of Flight (TOF) measurement (details in Section 3.4).

2.3 TRIGGER SYSTEM

The start of data acquisition is preceded by a two levels trigger system [41]. The first level trigger (T_1) is a fast trigger with a minimal delay which starts the acquisition at the front-end electronics. It requires two local energy deposits above threshold in the EMC (50 MeV on the barrel, 150 MeV on the end-caps) and hit multiplicity information from the drift chamber. The trigger time is determined by the first particle reaching the calorimeter and is synchronized with the DAΦNE radio frequency (RF) signal.

The second level trigger (T_2) uses information from both the drift chamber and the electromagnetic calorimeter. Both the triggers' decision can be vetoed if the events were recognized as Bhabha scattering or cosmic ray event (see Figure 2.4). For control purposes those events are accepted and saved as a dedicated downscaled sample. The background events from the Bhabha scattering, cosmic rays or machine background that survive the trigger requirements are rejected at the beginning of the offline reconstruction by the background filter. Without the background rejection at the trigger level the background rate would be almost 20 times greater than the ϕ meson production rate.

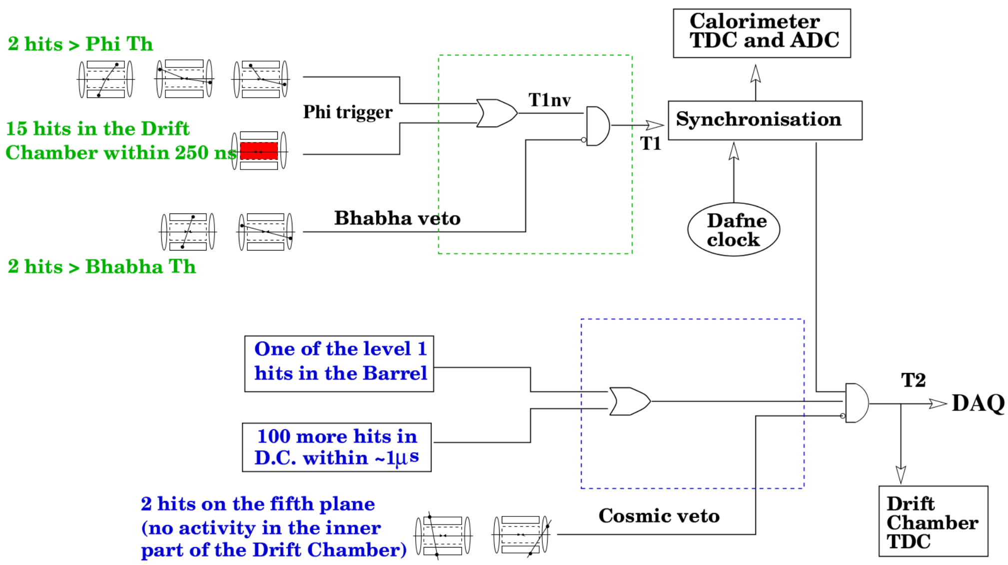

Figure 2.4: Diagram of the two-level trigger logic. It has been optimized to preserve the majority of $e^+e^- \to \phi$ decays, and provide efficient rejection of the two main sources of background: small angle Bhabha scattering and particles lost from DAΦNE beams. Both T_1 and T_2 triggers are based on the topology of energy deposits in the EMC and on the hit multiplicity in the DC. Figure adapted from Ref. [39].

2.3.1 *Determination of the global time offset*

The time interval between bunch crossings ($T_{bunch} = 2.715$ ns) is smaller than the time spread of the registered signals originating from $K_L K_S$ events that can reach 30-40 ns. The offline reconstruction procedure therefore has to determine the true bunch crossing time T_0 for each event and correct all times related to that event accordingly. In standard reconstruction algorithms the T_0 time is determined by using the information coming from the electromagnetic calorimeter. In the studied channel, since the K_S decay time is smaller than K_L interaction time in the calorimeter, the T_0 time has to be corrected in an offline analysis. Details will be given in Section 3.4.

2.4 OFFLINE RECONSTRUCTION FILTER AND EVENT CLASSIFICATION ALGORITHM

Signals gathered by the electronics are translated into quantities connected with the detector using the detector maps. Then information associated with the calorimeter is reconstructed first in order to produce the preliminary estimate of T_0 (see Section 2.3.1). The events identified as Bhabha scattering, cosmic rays and machine background are rejected based on the reconstructed information. Next, the CPU-intensive procedures are invoked: reconstruction of the charged particles' tracks and vertices in the drift chamber.

All collected events are classified into dedicated streams:

- **KPM** $\phi \to K^+K^-$,
- **KSL** $\phi \to K_L K_S$,
- **RPI** $\phi \to \rho\pi$,
- **RAD** $\phi \to radiatives \ \ (\eta\gamma, \eta'\gamma, \pi^0\gamma...)$,
- **CLB** Bhabha and cosmic events used as calibration samples,
- **UFO** UnidentiFied Objects.

The main selection criteria are based on a robust set of cuts in order to allow users to perform more sophisticated analyses [42–44]. To maximize streaming efficiency a single event can be tagged by more than one algorithm. At the same time, the streams overlap is kept below the one per cent level. For the efficiency estimation procedure every 10^{th} reconstructed event is stored, regardless of decisions of the classification algorithm.

The data sample used for this analysis has been processed and filtered with the KLOE standard reconstruction software and the event classification procedure. The simulated data samples are based on the Monte Carlo (MC) GEANFI program [45]. The program included a full description of the KLOE detector simulating the responses of all detectors and it accounts for their efficiency and resolutions. Monte Carlo simulations took into account - run by run - data taking conditions such as the ϕ momentum, beam spot size and position, background levels, trigger thresholds and dead channels.

3 REGISTRATION OF THE $\phi \to K_L K_S \to K_L(crash)\pi e \nu$ PROCESSES AT KLOE

The charge asymmetry for the short-lived neutral kaon is given by:

$$A_S = \frac{N^+/\epsilon^+ - N^-/\epsilon^-}{N^+/\epsilon^+ + N^-/\epsilon^-}, \tag{3.1}$$

where N^+ and N^- are the numbers of observed $K_S \to \pi^- e^+ \nu$ and $K_S \to \pi^+ e^- \bar{\nu}$ decays, respectively, while ϵ^+ and ϵ^- are the corresponding analysis efficiencies. Negative and positive charged pions interact differently in the detector material, therefore the efficiency is separately estimated for $\pi^- e^+ \nu$ and $\pi^+ e^- \bar{\nu}$ final charge states. It should be noted that the A_S value depends only on the ratio of π^+/π^- (e^+/e^-) efficiencies and not on the absolute values. The ratio $\epsilon(\pi^+)/\epsilon(\pi^-)$ - for the part which depends on the different nuclear interactions of positive and negative pions - has been determined directly from data using a control sample because the MC simulation was not fully reliable on this point. On the other hand, e^+ and e^- interactions are charge independent (aside of the negligible contribution of e^+ annihilation in flight) so the MC can safely be used for their estimate.

The measurement of A_S requires a very pure K_S beam which can only be realised exploiting the entangled neutral kaons pairs produced at a ϕ-factory. This property is used in the so-called tagging technique - identification of $K_L(K_S)$ meson on one side allows to select a $K_S(K_L)$ meson on the other side of the ϕ meson decay point (see Figure 3.1). The performed analysis is based on an identification of K_S through the detection of K_L interaction in the calorimeter. In order to select semileptonic decays of K_S mesons, an additional kinematic selection is applied. It starts from a requirement of a vertex formation by tracks of two oppositely charged particles near the ϕ meson decay point. In the next step, the signals from drift chamber and Time of Flight technique are applied to improve signal over background ratio and to attribute the recorded tracks and EMC interactions to particles from the semileptonic decay.

3.1 K_L CRASH SELECTION

About 60% of produced K_L mesons reach the calorimeter and deposit energy there, which is referred to as K_{crash}. Due to that, the selection of K_L candidates takes into account only particle interactions in EMC (commonly referred to as calorimeter clusters) with energy

$$E_{clu}(K_{crash}) \geqslant 100 \text{ MeV}. \tag{3.2}$$

It is also required that the cluster is not connected with any track reconstructed in drift chamber. The obtained energy distribution of K_{crash} is shown in Figure 3.2. The visible discrepancy between data (dashed histogram) and MC simulations (thin,

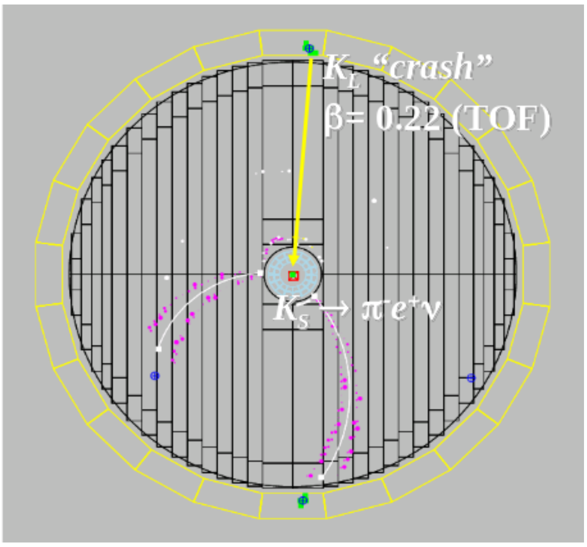

Figure 3.1: Transverse view of an exemplary signal event. The figure was obtained using the Event Display for the KLOE experiment [46]. The neutral kaons identification is simplified by the difference in its mean life times - K_S decays close to the interaction point (IP). Therefore in the analysis the position of a K_L vertex can be limited to distances larger than a few τ_{K_S} from the IP. In the conducted analysis the K_S is identified using the K_L interaction in the calorimeter. In the next step, the semileptonic decays of K_S mesons are selected by requiring vertex near the IP. Further sample cleaning is provided by applying kinematical cuts and the Time of Flight technique.

solid histogram) is due to a simplified description of the calorimeter in the simulation. Therefore, the energy distribution was modified by the phenomenological correction [47]:

$$E_{clu}^{new}(K_{crash}) = E_{clu}^{old}(K_{crash}) \cdot (p1 + Int(E_{clu}^{old} - 100) \cdot p2), \tag{3.3}$$

where $E_{clu}^{old}(K_{crash})$ and $E_{clu}^{new}(K_{crash})$ stands for cluster energy before and after correction, Int returns an integer part of the expression, while values of $p1$ and $p2$ were obtained from previous KLOE analysis and are equal to 1.025 and 0.0003, respectively [48].

Since the angular distribution of kaon emission is described by characteristic p-wave angular distribution: $\frac{dN}{d\Omega} \propto \sin^2\theta$, where θ is a polar angle, most of the kaons are emitted in the direction perpendicular to the beam axis. Therefore, a part of background is rejected by choosing K_L clusters only in the barrel part of the calorimeter.

In the next step, for each cluster candidate the velocity of the contributing particle is calculated as:

$$\beta = \frac{R_{clu}}{c \cdot t_{clu}}, \tag{3.4}$$

where R_{clu} and t_{clu} denote the distance and time of flight of the K_L between the interaction point (obtained run by run from Bhabha events) and cluster position respectively, and c is the speed of light. In the ϕ meson rest frame K_L mesons have

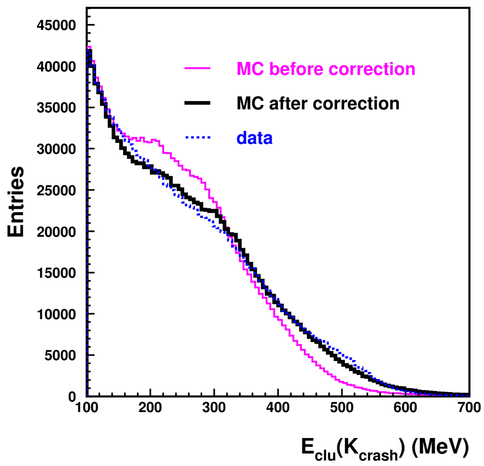

Figure 3.2: Distribution of K_L crash energy for data (dashed histogram) and Monte Carlo simulations before (thin solid histogram) and after (thick solid histogram) the correction described in text. Figure was obtained using a part of the total statistics.

low velocity $\beta \sim 0.22$. To compare the obtained β value with the expected one, the transformation to the ϕ rest frame is applied [47, 49]:

$$\beta^* = \frac{\sqrt{\beta^2 + \beta_\phi^2 + 2\beta\beta_\phi \cos\alpha}}{1 - \beta_\phi\beta\cos\alpha}, \tag{3.5}$$

where α is the angle between the ϕ meson momentum vector and the direction connecting the interaction point with the cluster position.

The obtained β^* distribution (Figure 3.3, left) peaks at two different values due to the procedure used to determine T_0, which assumes the first cluster to be generated by a prompt photon which does not occur in case of the semileptonic decays. If the T_0-cluster is generated by the fastest pion, which has a time of flight of ~ 10 ns (instead of $6-7$ ns for a prompt photon), then the bunch crossing number differs from the correct value by (-1). Example of simulated β^* distribution for different bunch numbers is shown in Figure 3.3, right. Hence, the applied cut

$$0.18 < \beta^* < 0.27 \tag{3.6}$$

is chosen to contain both peaks for further analysis.

If more than one cluster fulfilled the above criteria then the one with the smallest time of arrival (t_{clu}) is chosen as corresponding to the interaction of the K_L meson.

3.1.1 *Kaons momentum determination*

After K_L identification, its momentum is determined by considering the two body decay in the ϕ rest frame:

$$p_K = \frac{(E_K^{CM}/\gamma_\phi)\beta^{CM}\cos\theta + \sqrt{(\beta^{CM})^2 M_K^2 \cos^2\theta + (E_K^{CM}/\gamma_\phi)^2 - M_K^2}}{1 - (\beta^{CM})^2\cos^2\theta}, \tag{3.7}$$

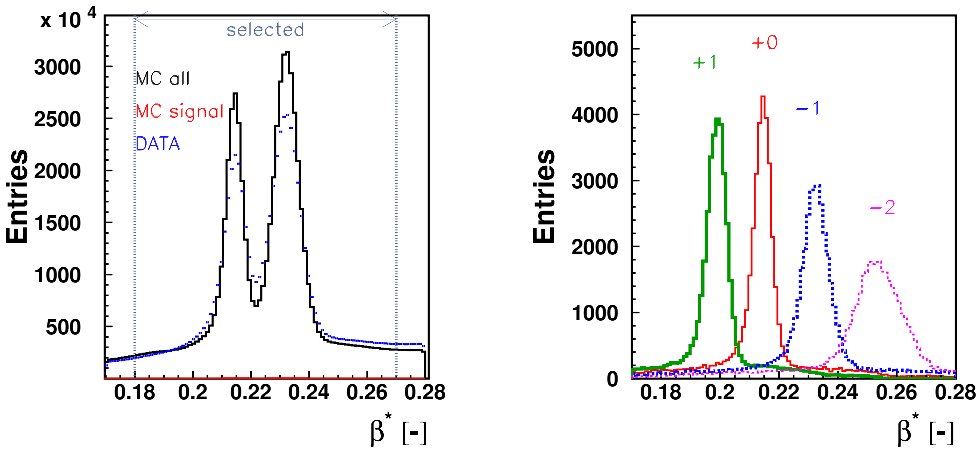

Figure 3.3: Left: distribution of velocity of the tagging K_L meson for experimental (blue points) and simulated histograms. Solid black line represents all simulated events, while red dashed corresponds to the semileponic decay. The double peak structure results from the bunch number assignment during time reconstruction. Right: Monte Carlo simulation showing dependency between position of peak structure and assigned bunch crossing number.

where the E_K^{CM} is the kaon energy in the center of mass and θ is the angle of the kaon with respect to the ϕ meson boost direction.

The momentum components of both kaons are given by:

$$\vec{p}_{K_1} = p_K \frac{\vec{x}_K - \vec{x}_\phi}{|\vec{x}_K - \vec{x}_\phi|}, \tag{3.8}$$

$$\vec{p}_{K_2} = \vec{p}_\phi - \vec{p}_{K_1}, \tag{3.9}$$

where $\vec{x}_K$ and $\vec{x}_\phi$ are position of K_L interaction vertex and ϕ meson production point, respectively.

In order to do a transformation from the ϕ meson center of mass frame to the laboratory frame the position and momentum vector of the ϕ meson and the K_L cluster position are needed. The ϕ meson parameters are obtained run by run from Bhabha scattering events.

3.2 CORRECTION OF MOMENTA DISTRIBUTION IN MONTE CARLO SIMULATION

To improve Monte Carlo simulations with data agreement for the final distribution the reconstructed MC track momentum components p_i have been smeared using three Gaussian functions:

$$p_i^{new} = p_i \times (1 + \alpha_p) \times (1 + \Delta \cdot \sum_{j=1}^{3} f_j \cdot G(0, \sigma_j)), \qquad (i = x, y, z) \tag{3.10}$$

where $G(0, \sigma_j)$ is the Gaussian distribution with zero mean and standard deviation σ_j, f_j is its amplitude, while Δ is the fractional uncertainty on the track curvature.

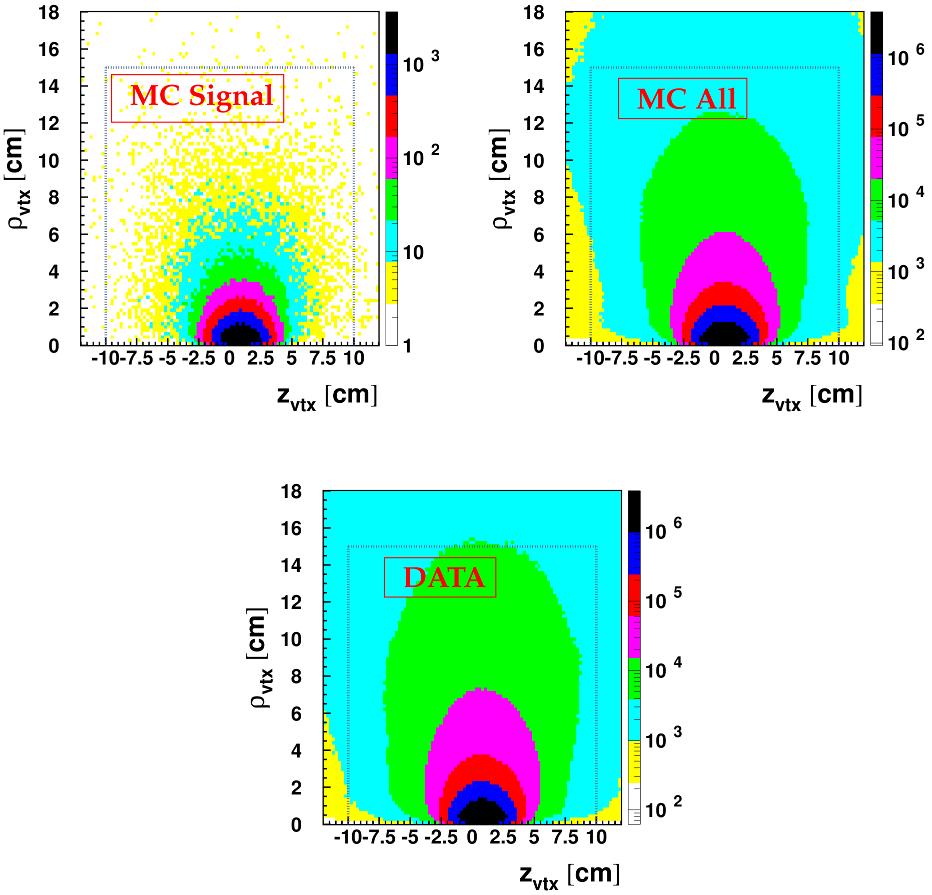

Figure 3.4: Distributions of radial and z coordinates of vertex position for selected events. Top panels show MC distributions for $K_S \to \pi e \nu$ and full MC sample, respectively. Bottom panel shows the result for collected data. Dashed line represents the applied cuts which preserve $\sim 95\%$ of the signal events.

The momentum shift α_p and the Gaussian parameters are tuned using the $K_L \to \pi e \nu$ control sample (see Section 3.6). The fit yields $f_1 = 96\%$, $\sigma_1 = 0.34$, $f_2 = 3.2\%$, $\sigma_2 = 9.74$, $f_3 = 0.8\%$, $\sigma_3 = 71.2$ and $\alpha_p = 1.37 \cdot 10^{-4}$. The smearing scheme was adapted from [50].

3.3 SELECTION OF $K_S \to \pi e \nu$ EVENTS

Selection of semileptonic events starts from a requirement of two oppositely charged particles with tracks forming a vertex close to the Interaction Point (IP) (see Figure 3.4):

$$\begin{aligned} \rho_{vtx} &< 15 \text{ cm}, \\ |z_{vtx}| &< 10 \text{ cm}, \end{aligned} \tag{3.11}$$

where ρ_{vtx} is a radial distance in the $x - y$ plane between the selected vertex and the e^+e^- interaction point. The main background source for $K_S \to \pi e \nu$ decays is the $K_S \to \pi^+\pi^-$ process with misidentification of π as e, since $BR(K_S \to \pi^+\pi^-)$ is

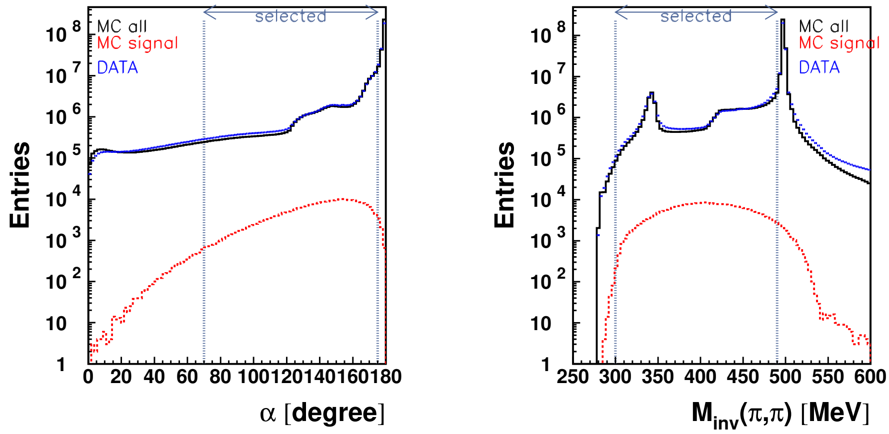

Figure 3.5: Left: Simulated distribution of the angle between charged secondaries in K_S rest frame. Right: Simulated distribution of invariant mass calculated under the assumption that both registered particles were pions. In both figures black solid lines represent all events, red dashed lines show semileptonic decays and blue points are the collected data. Vertical dashed lines represent the cuts described in the text.

around 10^4 times larger than for the signal events. The first cut applied to reject $K_S \to \pi^+\pi^-$ events at preselection stage is:

$$70^\circ < \alpha < 175^\circ, \tag{3.12}$$

where α is the angle between momenta of charged secondaries in K_S rest frame. The obtained α distribution is shown in the left panel of Figure 3.5. In case of two body decay (such as $K_S \to \pi^+\pi^-$) α takes the value of $\sim 180^\circ$ and in case of three body decay ($K_S \to \pi e \nu$) it is spanned over a large range (dashed histogram). The applied cut allows to reduce the remaining $K_S \to \pi\pi$ background by 80% while only 3% of signal is rejected. The next cut is on an invariant mass $M_{inv}(\pi, \pi)$, calculated using momenta of the particles which track form a vertex, assuming that both particles were pions:

$$300 < M_{inv}(\pi, \pi) < 490 \text{ MeV}. \tag{3.13}$$

The obtained distribution is shown on the right side of Figure 3.5. This requirement reduces remaining $K_S \to \pi\pi$ decays by 53% while only 4% of signal is rejected. Both tracks reconstructed in the drift chamber are associated with neighbouring clusters in calorimeter (TCA - Track to Cluster Association). The TCA procedure extrapolates each of the tracks from the last registered position in the drift chamber toward the calorimeter surface and determines the impact point.

3.4 PARTICLE IDENTIFICATION WITH THE TIME OF FLIGHT METHOD

The Time of Flight technique aims at rejection of the background, which at this stage of analysis is still mainly due to $K_S \to \pi^+\pi^-$ events, and at identification of the final charge states ($\pi^\pm e^\mp$). For each particle, the time difference $\delta_t(X)$ is obtained from the measured time of associated cluster ($t_{cl} - T_0$) and expected time of flight calculated under the m_X mass hypothesis:

$$\delta_t(X) = (t_{cl} - T_0) - \frac{L}{c \cdot \beta(X)}, \quad \beta(X) = \frac{p}{\sqrt{p^2 + m_X^2}}. \tag{3.14}$$

where L is the total length of particle trajectory determined from the DC and p is particle momentum. Since at this stage the ϕ decay time (T_0) is not known with sufficient precision, the following T_0-independent difference is introduced:

$$\delta_t(X,Y) = \delta_t(X)_1 - \delta_t(Y)_2 \ , \tag{3.15}$$

where the mass hypotheses m_X and m_Y are used for tracks 1 and 2, respectively. Since for the correct mass hypotheses assignments the value $\delta_t(X,Y)$ is close to zero, the condition

$$|\delta_t(\pi,\pi)| > 1.5 \text{ ns} \tag{3.16}$$

is applied for further $K_S \to \pi^+\pi^-$ events rejection (see Figure 3.6). The remaining

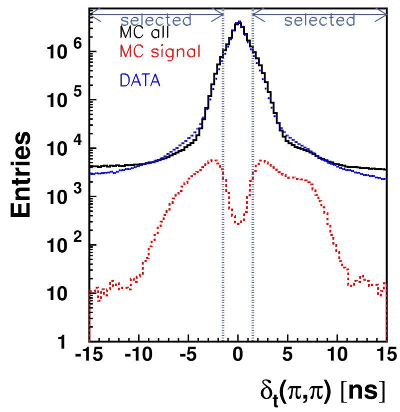

Figure 3.6: Distribution of the $\delta_t(\pi,\pi)$ variable. Solid black line represents all simulated events, while red dashed line shows the semileponic decay. Blue dots show data location and vertical dashed lines represent the cut described in text.

pairs of tracks are tested under pion-electron $\delta_t(\pi,e)$ and electron-pion $\delta_t(e,\pi)$ hypothesis (see Figure 3.7):

$$\begin{gathered} |\delta_t(e,\pi)| < 1.3 \text{ ns} \ \wedge \ \delta_t(\pi,e) < -3.4 \text{ ns} \\ \text{or} \\ \delta_t(e,\pi) > 3.4 \text{ ns} \ \wedge \ |\delta_t(\pi,e)| < 1.3 \text{ ns} \end{gathered} \tag{3.17}$$

Once particle identification has been performed, the time differences $\delta_t(e)$ and $\delta_t(\pi)$ are reevaluated using the identified particle masses and subtracting the T_0 of the event:

$$T_0 = Nint\left(\frac{\delta_t(m_\pi) + \delta_t(m_e)}{2 \cdot T_{bunch}}\right) \times T_{bunch}, \tag{3.18}$$

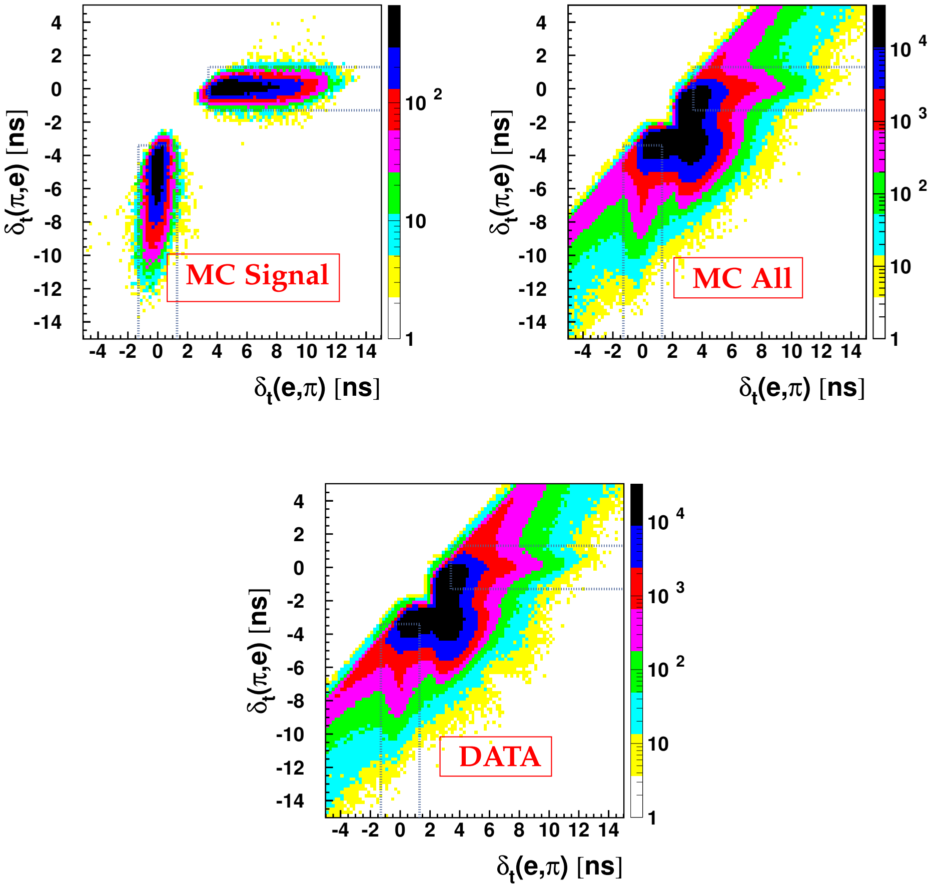

Figure 3.7: Distributions of time differences $\delta_t(\pi, e)$ vs $\delta_t(e, \pi)$ for $K_S \to \pi e\nu$ events (top, left), all simulated events (top, right) and data (bottom). Events located in one of the regions delimited by the dashed lines are selected. In case of semileptonic decays the $\delta_t(e, \pi)$ ($\delta_t(\pi, e)$) variable takes value close to zero.

where $Nint$ stands for the nearest integer and $T_{bunch} = 2.715$ ns is the minimum bunch crossing period. Events are then selected within the circle in the $\delta_t(e) - \delta_t(\pi)$ plane:

$$\left(\frac{\delta_t(e) - 0.07 \text{ ns}}{0.6 \text{ ns}}\right)^2 + \left(\frac{\delta_t(\pi) - 0.13 \text{ ns}}{0.6 \text{ ns}}\right)^2 < 1 \tag{3.19}$$

as shown in Figure 3.8. Position of the center was determined from the data sample. This cut keeps the number of background events selected for normalization under control. Details of the normalization procedure are presented in the next Section.

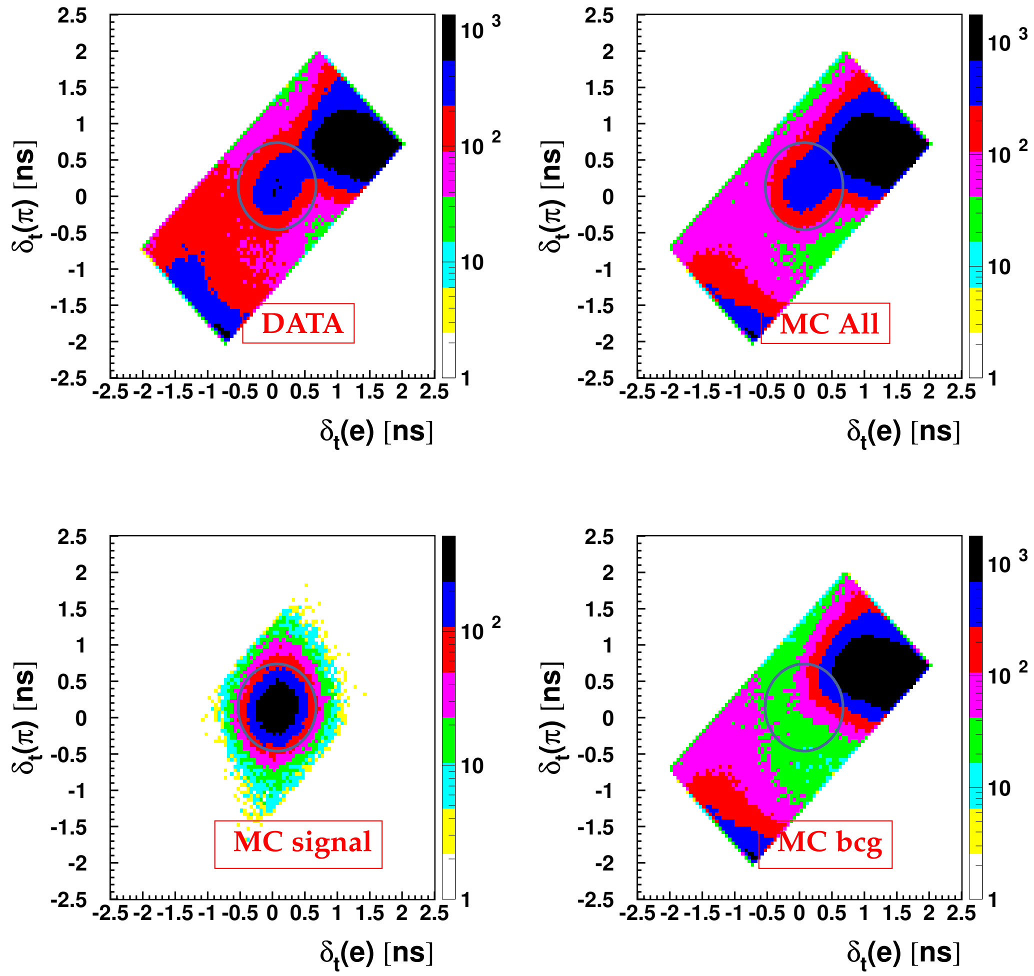

Figure 3.8: Distributions of the time difference between expected and observed time of flight for the particles identified as pion ($\delta_t(\pi)$) and electron ($\delta_t(e)$) for experimental data (top-left), total MC events (top-right), MC $K_S \to \pi e \nu$ events (bottom-left) and MC background events (bottom-right). Events within the circle are retained for further analysis.

3.5 SIGNAL EXTRACTION

After the presented event selection criteria, the remaining residual background components are:

- $K_S \to \pi^+\pi^-$, where one of the pion tracks is badly reconstructed and classified as an electron by the Time of Flight procedure,
- $K_S \to \pi^+\pi^- \to \pi\mu$, where π decay occurred before entering the drift chamber,
- $K_S \to \pi^+\pi^-\gamma$,
- other, mainly $\phi \to K^+K^-$ decays.

The best separation between signal and background components is provided by the variable:

$$\begin{aligned} M^2(e) &= E^2(e) - p^2(e) \\ &= (E_{K_S} - E(\pi) - E_{miss})^2 - p^2(e) \\ &= (E_{K_S} - E(\pi) - p_{miss}(\pi, e))^2 - p^2(e), \end{aligned} \tag{3.20}$$

$$p_{miss} = \sqrt{\sum_{i=x,y,z} (p_{K_S,i} - p_{e,i} - p_{\pi,i})^2}, \tag{3.21}$$

presented in Figure 3.9. Its sensitivity lies in the fact that during the Time of Flight procedure a wrong mass hypothesis is usually assigned to the particle classified as an electron. So, muons (from $\pi\mu$ background category) or badly reconstructed pions (from $\pi\pi$ background category) can be separated based on their mass difference. In case of a proper assignment, E_{miss} and p_{miss} correspond to the energy and momentum of a neutrino.

The signal yield is estimated by fitting the $M^2(e)$ data distribution with the sum of the corresponding simulated distributions for signal and background channels with free normalization and accounting for a finite size of the Monte Carlo sample [51, 52]. In order to obtain a χ^2 distributed variable the log-likelihood is normalized as explained in Ref. [53].

The result of the fit for the signal events is 34579 ± 251 for $K_S \to \pi^-e^+\nu$ and 36874 ± 255 for $K_S \to \pi^+e^-\bar{\nu}$, with total $\chi^2/ndof = 118/109$, summing on the two final charge states (see Figure 3.9).

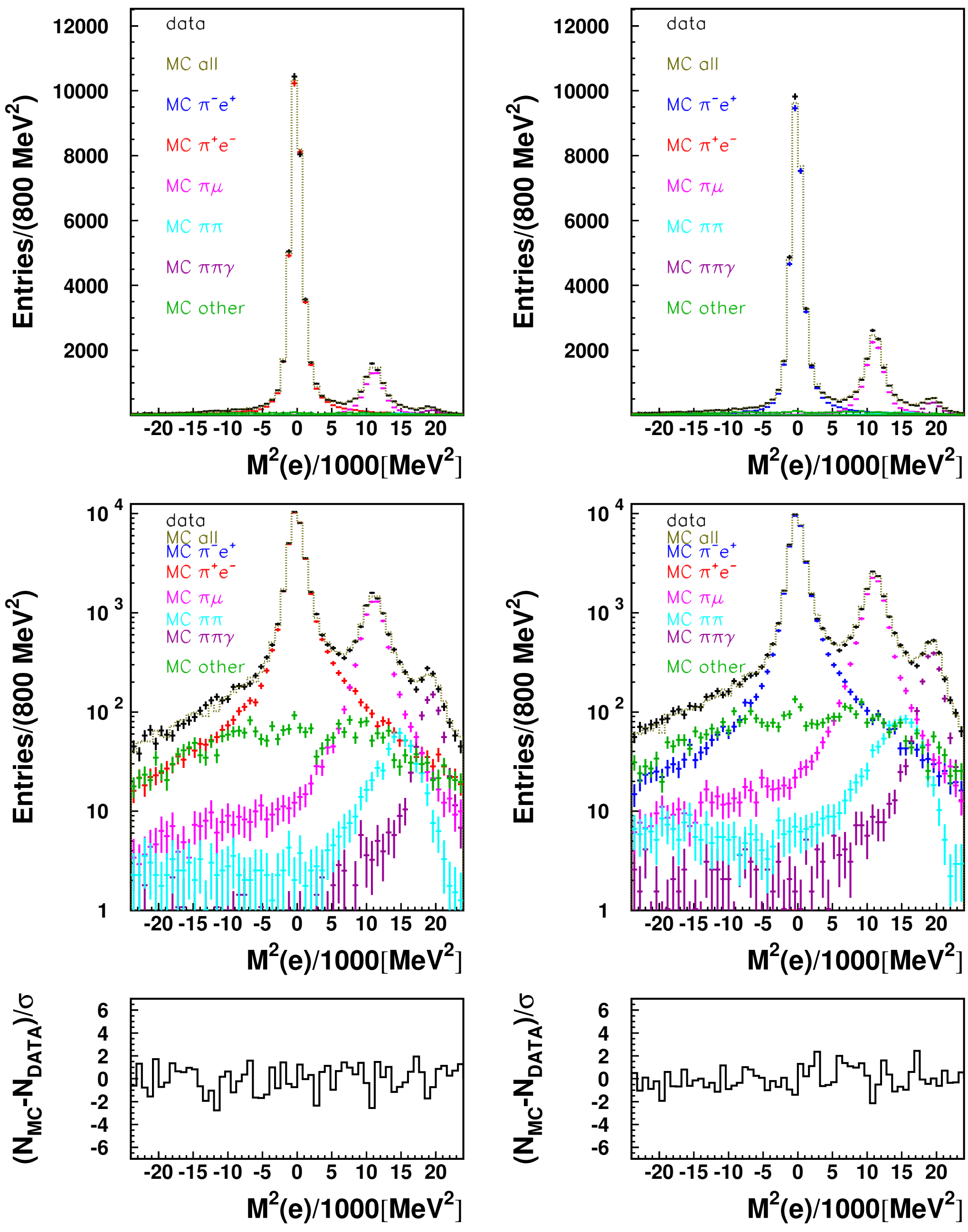

Figure 3.9: Distribution of the $M^2(e)$ variable (Eq. 3.21) for data (points) and MC simulations (solid line) of $M^2(e)$ variable after the normalization procedure described in the text for both final charge states ($\pi^+e^-\bar{\nu}$ - left panels, $\pi^-e^+\nu$ - right panels). Middle row is the logarithmic representation of plots in the top row. The bottom row presents spectra of residual errors of the fits.

3.6 SELECTION OF THE $K_L \rightarrow \pi e\nu$ CONTROL SAMPLE

The efficiencies of the selection of the semileptonic channels will differ due to different registration probabilities of positive and negative pions in the detector. To account for this effect a data sample of $K_L \rightarrow \pi e\nu$ decay, which is a dominant decay mode of K_L meson (see Table 2.1), is selected and used as a control sample. Moreover, the A_L value was estimated in order to rule out any possible bias in the analysis scheme.

The events of the control sample are tagged by the neutral K_S decay $K_S \rightarrow \pi^0\pi^0$. Selection of $K_S \rightarrow \pi^0\pi^0$ events is provided by the standard KLOE tagging algorithm [42, 43] which looks for clusters in the barrel of the electromagnetic calorimeter not associated to any tracks. The total deposited energy should be greater than 300 MeV and each of the candidates has to deposit energy between 20 MeV and 300 MeV. The last step is the evaluation of the K_S invariant mass m_K which should satisfy the $(390 < m_K < 600)$ MeV condition. The estimated efficiency is: $(60.0 \pm 0.3)\%$. No appreciable contamination is found from other ϕ meson decays and the machine background is kept at the level of 1%.

3.6.1 *Lepton charge asymmetry for long-lived kaon*

The selection of $K_L \rightarrow \pi e\nu$ was performed in the same way as the selection of $K_S \rightarrow \pi e\nu$ which was described in detail in Section 3.3 and 3.4. The normalization requires two scaling factors only (signal and background, see Figure 3.10), because the semileptonic channel is a main decay mode of K_L meson.

The purity $(S/(S+B))$ of the sample reaches 96.62%. The final number of selected events is 522834 ± 1106 and 544183 ± 1122 for $K_L \rightarrow \pi^- e^+ \nu$ and $K_L \rightarrow \pi^+ e^- \bar{\nu}$ decays, respectively. This allows to determine the value of lepton charge asymmetry for the long-lived kaon (analogously as in Equation 3.1) to be:

$$A_L = (1.7 \pm 2.7_{stat}) \cdot 10^{-3}, \tag{3.22}$$

which is consistent with the best measurement of this value provided by the KTeV [28] within one standard deviation.

3.6.2 *Sample selection for efficiency determination*

The events of the control sample are used to estimate the efficiencies for positive and negative pions. To this aim a single track selection scheme is developed and applied, after vertex reconstruction and cuts on the opening angle in the K_L rest frame and $M_{inv}(\pi, \pi)$, as described in Section 3.3.

At this stage we require that at least one track reaches the calorimeter with TCA. For this track the $\delta_t(e)$ and $\delta_t(\pi)$ variables are constructed (see Equation 3.14). A sample of electrons (positrons) is then selected by requiring (see Figure 3.11):

$$[(\delta_t(e) - 0.07 \text{ ns})/1.2 \text{ ns}]^2 + [(\delta_t(\pi) + 4 \text{ ns})/3.2 \text{ ns}]^2 < 1. \tag{3.23}$$

As the aforementioned procedure does not require extrapolation of the pion tracks towards the calorimeter, the selected sample is used for TCA and TOF

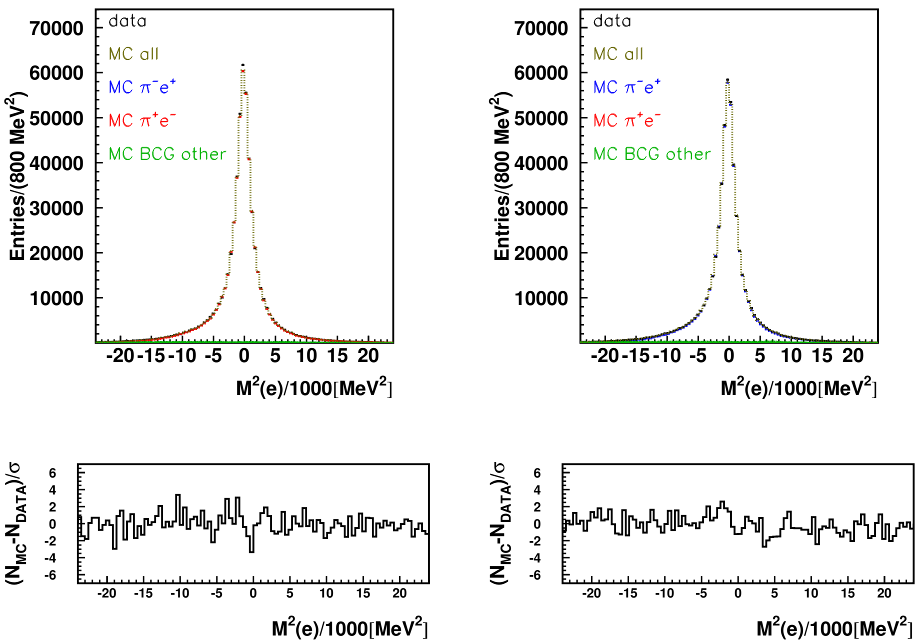

Figure 3.10: Results of the normalization procedure applied to the $K_L \to \pi e \nu$ control sample. Residual errors are shown in the bottom row. Right and left columns contain results for $\pi^+ e^- \bar{\nu}$ and $\pi^- e^+ \nu$, respectively.

efficiency evaluation separately for negative and positive pions. Details are given in Section 4.

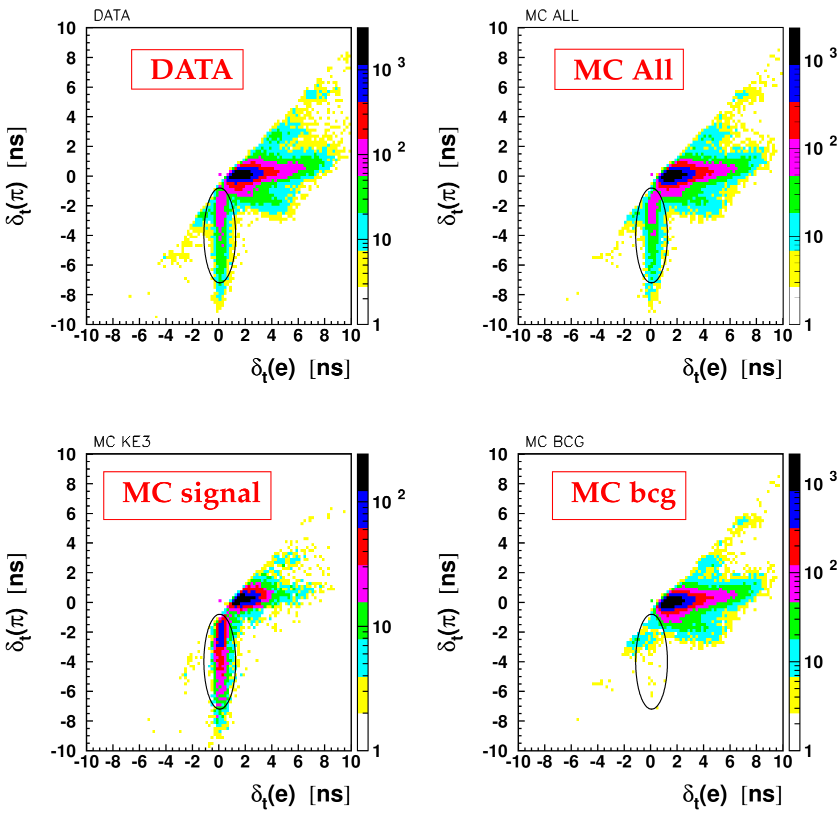

Figure 3.11: The $\delta_t(\pi)$ vs $\delta_t(e)$ distribution for all particles of the control sample with a calorimeter cluster associated to their corresponding DC track. Events within the ellipse contain $K_L \to \pi e\nu$ events and are chosen for efficiency estimation. Distributions were made for data (top left), total Monte Carlo events (top right), MC $K_L \to \pi e\nu$ events (bottom, left) and MC background events (bottom right). It should be noted that plots were made for a single track with two different mass hypotheses.

4 RESULTS

The analysis efficiency is estimated as follows:

$$\epsilon = \epsilon_{TEC} \cdot \epsilon_{TAG} \cdot \epsilon_{ANA}, \tag{4.1}$$

where ϵ_{TEC} stands for trigger and event classification efficiency, while ϵ_{TAG} and ϵ_{ANA} denote tagging and analysis efficiencies, respectively.

The analysis efficiency ϵ_{ANA} can be expressed as a product of four contributions:

- kinematical cuts (ϵ_{KC}): cuts on reconstructed vertex fiducial volume, opening angle α, and $M_{inv}(\pi, \pi)$ (see Section 3.3);
- Track to Cluster Association algorithm (ϵ_{TCA});
- Time of Flight cuts (ϵ_{TOF});
- fit range (ϵ_{FR}) of the $M^2(e)$ variable.

The efficiency ϵ_{TEC} is evaluated using downscaled minimum-bias data samples without event classification and background rejection filters applied. The estimation of ϵ_{TAG}, ϵ_{KC} and ϵ_{FR} are based on MC simulation. ϵ_{TOF} are determined using the $K_L \to \pi e \nu$ control sample with the method described in Section 4. ϵ_{TCA} consists of the product of $\epsilon_{TCA}(\pi^{\pm})$, evaluated from control sample, and $\epsilon_{TCA}(e^{\mp})$ determined from MC:

$$\epsilon_{TCA} = \epsilon_{TCA}^{KS}(\pi) \times \epsilon_{TCA}^{KS}(e) = \epsilon_{TCA}^{KL\ DATA}(\pi) \times \frac{\epsilon_{TCA}^{KS\ MC}(\pi)}{\epsilon_{TCA}^{KL\ MC}(\pi)} \times \epsilon_{TCA}^{KS\ MC}(e). \tag{4.2}$$

Then, the Time of Flight efficiency is determined using the $K_L \to \pi e \nu$ data control sample in a similar manner:

$$\epsilon_{TOF}^{KS} = \epsilon_{TOF}^{KL\ DATA} \times \frac{\epsilon_{TOF}^{KS\ MC}}{\epsilon_{TOF}^{KL\ MC}}. \tag{4.3}$$

The total efficiency is $(7.39 \pm 0.03)\%$ and $(7.81 \pm 0.03)\%$ for $K_S \to \pi^- e^+ \nu$ and $K_S \to \pi^+ e^- \bar{\nu}$, respectively. The evaluated efficiencies for the different analysis steps are presented in Table 4.1.

Using these efficiencies in Eq. 3.1 the result for A_S is:

$$A_S = (-4.9 \pm 5.7_{stat}) \times 10^{-3}. \tag{4.4}$$

4.0.1 *Stability of the final result in time*

In order to study A_S variation during the measurement time, the whole analysed sample was divided into ten subsamples equal in luminosity. For each of them

Table 4.1: Efficiencies (%) for the different analysis steps.

Efficiency (%)	$K_S \to \pi^- e^+ \nu$	$K_S \to \pi^+ e^- \bar{\nu}$
trigger and event classification (ϵ_{TEC})	99.80 ± 0.02	99.80 ± 0.02
K_S tagging (ϵ_{TAG})	36.54 ± 0.05	36.67 ± 0.05
kinematical cuts (ϵ_{KC})	75.60 ± 0.07	75.62 ± 0.07
Track to Cluster Association (ϵ_{TCA})	42.22 ± 0.08	41.85 ± 0.08
Time of Flight (ϵ_{TOF})	64.03 ± 0.19	67.96 ± 0.18
Fit range (ϵ_{FR})	99.16 ± 0.03	99.17 ± 0.02

the $A_S(i)$ was determined separately (see Figure 4.1). The mean value of $A_S(i)$ is consistent with the result obtained by analyzing the whole data set. Moreover, no time-dependent effect is visible in analysis efficiencies (see Figure 4.2). Due to different probability of interaction of negative and positive pions in the detector material (see Section 3), the discrepancy between efficiencies for both final charge states is observed.

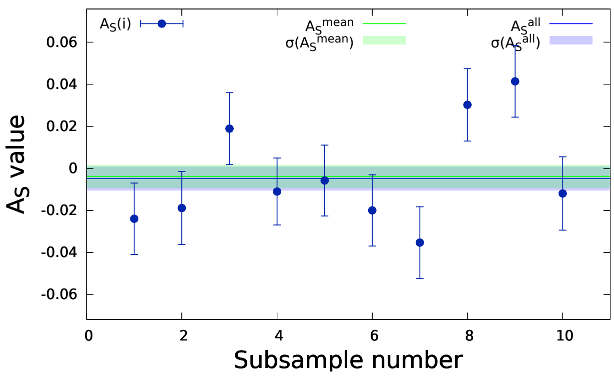

Figure 4.1: Value of the lepton charge asymmetry determined for the short-lived kaon in different data taking periods (blue points). Green horizontal line represents the mean value of obtained $A_S(i)$, while the blue horizontal line indicates the result obtained by analysis of the whole sample.

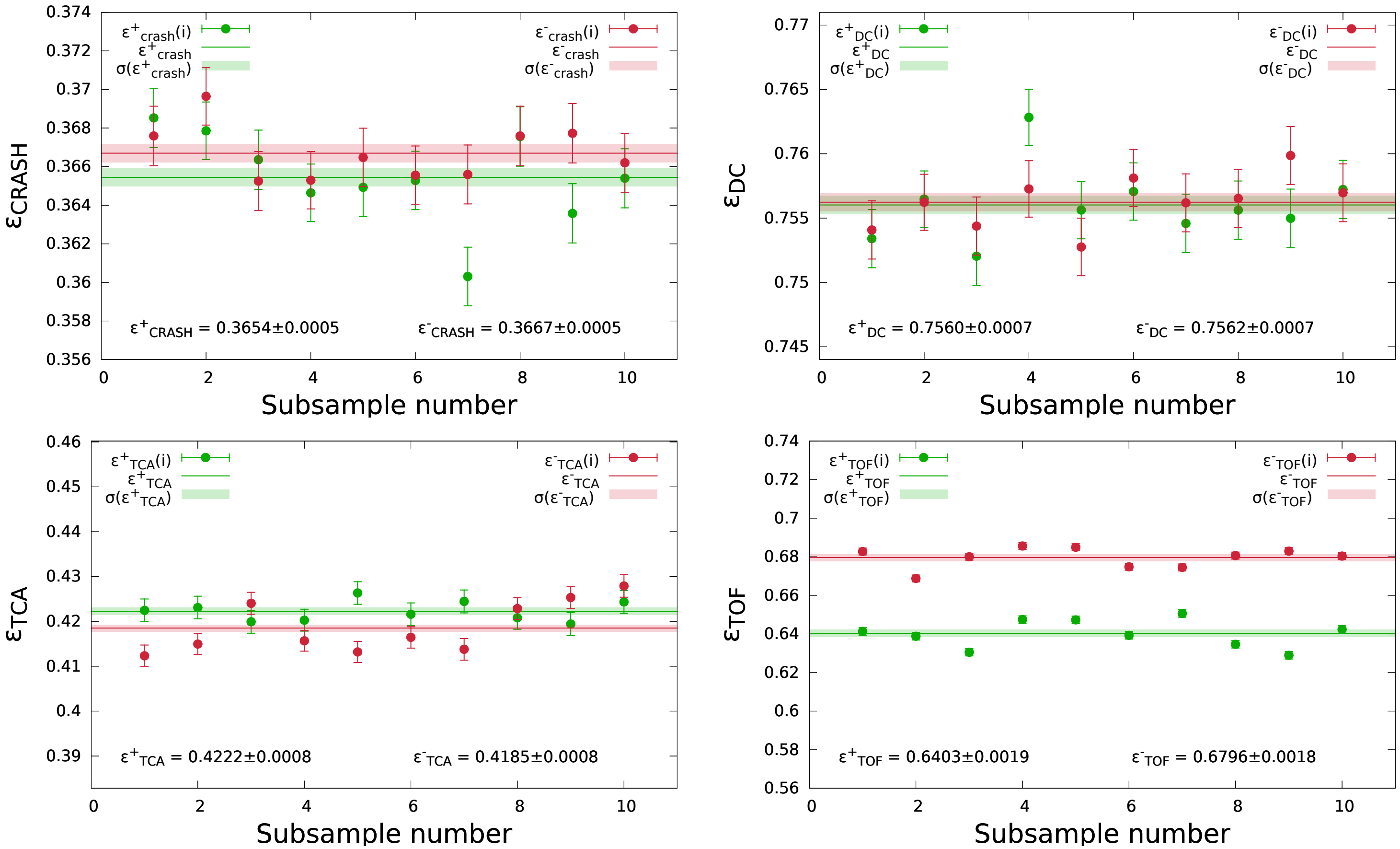

Figure 4.2: Efficiencies of the tagging procedure (top left), DC selection (top right), Track to Cluster association (bottom left) and Time of Flight analysis (bottom right) obtained in each subsample (points) compared with values obtained for the whole sample (horizontal lines). Positive and negative final charge states are indicated by green and red colors, respectively.

4.1 SYSTEMATIC UNCERTAINTIES ON A_S

In order to estimate the contributions to the systematic uncertainty of the result, the full analysis chain is repeated varying all the analysis cut values of selection variables by $+/-$ an amount comparable to their experimental resolution. The contributions from the stability of $M^2(e)$ distribution fit, momenta smearing, trigger and event classification procedures are also estimated separately.

The systematic uncertainties are classified into the following groups (see Table 4.2):

- Trigger and event classification:
  - Systematic effects originating from the trigger and the event classification procedure are estimated with prescaled data samples (with a prescaling factor of 1/20). The analysis of the prescaled samples follows the standard analysis chain. The systematic contribution (σ_{TEC}) is estimated to be 0.28×10^{-3}.
- Tagging and preselection:
  - The K_L deposited energy cut (see Eq. 3.2) is changed to the values:
    $E_{clu}(crash) = \{95, 105, 110, 115, 150, 200\}$ MeV.
    The stability of the result is checked within this range. The systematic uncertainty is evaluated by changing the cut by ± 5 MeV.
  - The β^* interval (see Eq. 3.6) is enlarged or shrunk by 0.02 (1σ) on each side:
    $0.18 \mp 0.02 < \beta^* < 0.27 \pm 0.02$.
    The stability of the result is checked up to a variation of $\pm 5\sigma$.
  - The z_{vtx} and ρ_{vtx} cuts for the reconstructed $K_S \to \pi e \nu$ decay vertex position (see Eq. 3.11) are each independently varied by ± 0.2 cm $(\pm 1\sigma)$. The stability of the result is checked against a variation of $\pm 5\sigma$.
  - The range of the opening angle α of the charged secondaries in the K_S rest frame (see Eq. 3.12) is enlarged or shrunk by $2°$ (1σ) on each side:
    $70 \mp 2° < \alpha < 175 \pm 2°$.
    The stability of the result is checked up to a variation of $\pm 5\sigma$ with the constraint of the upper bound not exceeding $180°$.
  - The $M_{inv}(\pi, \pi)$ interval (see Eq. 3.13) is enlarged or shrunk by 1 MeV (1σ) on each side:
    300 ∓ 1 MeV $< M_{inv}(\pi, \pi) < 490 \pm 1$ MeV.
    The stability of the result is checked up to a variation of $\pm 5\sigma$.
- Time of flight selection:
  - The $|\delta_t(\pi, \pi)|$ cut (see Eq. 3.16) is varied by ± 0.1 ns. The stability of the result is checked up to a variation of ± 0.4 ns.
  - The regions for the selection of the signal in the $\{\delta_t(e, \pi), \delta_t(\pi, e)\}$ plane (see Eq. 3.17) are enlarged or shrunk by varying the cuts of ± 0.1 ns:
    $[|\delta_t(e, \pi)| < 1.3 \pm 0.1$ ns, $\delta_t(\pi, e) < -3.4 \pm 0.1$ ns$]$

or
$[\delta_t(e,\pi) > 3.4 \mp 0.1$ ns, $|\delta_t(\pi,e)| < 1.3 \pm 0.1$ ns$]$.
The stability of the result is checked up to variations of ± 0.4 ns.

  – The circular region for selection of the signal in the $\{\delta_t(e), \delta_t(\pi)\}$ plane (see Eq. 3.19) is enlarged or shrunk by varying its radius of ± 0.1 ns. The stability of the result is checked for variations ranging from -0.3 ns to $+0.4$ ns.

- Momenta smearing:
  – The $K_L \to \pi e \nu$ control sample is divided into ten subsamples equal in luminosity. The momenta smearing parameters are tuned separately for each subsample and obtained results are consistent within systematical uncertainty. From the standard deviation of the results the systematic contribution (σ_{MS}) is estimated to be 0.58×10^{-3}.

- Fit procedure:
  – The systematic uncertainty from the histogram bin width σ_{HBW} is determined by varying the bin width from 0.8 to 1.6 MeV$^2/1000$ (this variation corresponds to the $M^2(e)$ resolution evaluated from MC). σ_{HBW} is estimated to be 0.61×10^{-3}. The stability of the result is checked for variations of the bin width from 2σ to 5σ.
  – The systematic uncertainty from the fit range is evaluated by varying it from $[-24 : 24]$ MeV$^2/1000$ to $[-28 : 28]$ MeV$^2/1000$ or $[-20 : 20]$ MeV$^2/1000$. The stability of the fit procedure is checked for histogram ranges from $[-36 : 36]$ MeV$^2/1000$ to $[-12 : 12])$ MeV$^2/1000$, while keeping the nominal bin size.

The total systematic uncertainty is estimated as the sum in quadrature of the contributions listed above and reported in Table 4.2.

4.2 CHARGE ASYMMETRY FOR SHORT-LIVED KAON AND TEST OF CPT SYMMETRY

The value of the $K_S \to \pi e \nu$ charge asymmetry has been measured with the KLOE detector based on the data sample of 1.63 fb^{-1} integrated luminosity. The final value:

$$A_S = (-4.9 \pm 5.7_{stat} \pm 2.6_{syst}) \times 10^{-3}, \tag{4.5}$$

is consistent with the previous determination performed by the KLOE group [14] and improves its statistical accuracy by a factor of almost two.

Due to similar analysis schemes, parts of the systematical uncertainty of both KLOE measurements related to the applied cuts are correlated. Taking this information into account, the combined result of the reported measurement and the previous result is:

$$A_S = (-3.8 \pm 5.0_{stat} \pm 2.6_{syst}) \times 10^{-3}. \tag{4.6}$$

Table 4.2: Summary of contributions to the systematic uncertainty on A_S.

Contribution		Systematic uncertainty (10^{-3})
Trigger and event classification	σ_{TEC}	0.28
Tagging and preselection	$E_{clu}(crash)$	0.55
"	β^*	0.67
"	z_{vtx}	0.01
"	ρ_{vtx}	0.05
"	α	0.46
"	$M_{inv}(\pi,\pi)$	0.20
Time of flight selection	$\delta_t(\pi,\pi)$	0.71
"	$\delta_t(e,\pi)$ vs $\delta_t(\pi,e)$	0.87
"	$\delta_t(e)$ vs $\delta_t(\pi)$	1.82
Momenta smearing	σ_{MS}	0.58
Fit procedure	σ_{HBW}	0.61
"	Fit range	0.49
Total		2.6

The sum and difference of A_S and A_L allow to search for possible violation of the $\mathcal{CPT}$ symmetry, either in the decay amplitudes or in the mass matrix. Using the A_L result from KTeV [28] with the KLOE A_S value, determined in this work 4.6, the results are:

$$(A_S - A_L)/4 = Re(\delta_K) + Re(x_-) = (-1.8 \pm 1.4) \times 10^{-3}, \tag{4.7}$$
$$(A_S + A_L)/4 = Re(\epsilon_K) - Re(y) = (-0.1 \pm 1.4) \times 10^{-3}. \tag{4.8}$$

Using $Re(\delta_K) = (2.5 \pm 2.3) \times 10^{-4}$ [36] and $Re(\epsilon_K) = (1.596 \pm 0.013) \times 10^{-3}$ [54] the $Re(x_-)$ and $Re(y)$ parameters are extracted:

$$Re(x_-) = (-2.0 \pm 1.4) \times 10^{-3}, \tag{4.9}$$
$$Re(y) = (1.7 \pm 1.4) \times 10^{-3}. \tag{4.10}$$

The obtained $Re(x_-)$ and $Re(y)$ values are in agreement with the previous results but the uncertainty of the result from this thesis is by almost a factor of two smaller with respect to the former measurements [14, 36]. The obtained result agrees with the $\mathcal{CPT}$ symmetry invariance. Improvements are expected in the future with the analysis of the additional ~ 5.5 fb^{-1} of data collected by the KLOE-2 experiment [55–57].

Part II

FEASIBILITY STUDY OF o-Ps $\rightarrow 3\gamma$ MEASUREMENT WITH THE J-PET DETECTOR

5

J-PET DETECTOR

The Jagiellonian Positron Emission Tomograph (J-PET) is a cylindrically shaped detector built from plastic scintillators (see Figure 5.1). The novel concept of using

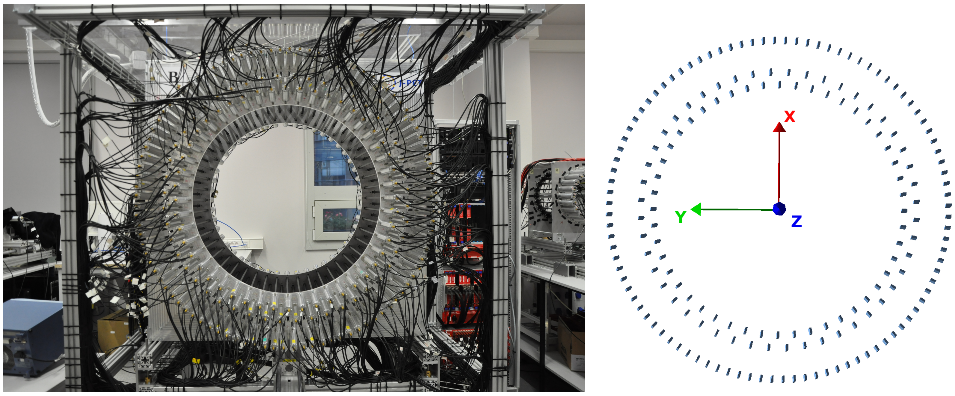

Figure 5.1: **Left:** Photo of the Jagiellonian Positron Emission Tomograph. The J-PET detector is made of three cylindrical layers of EJ-230 plastic scintillator strips (black) and Hamamatsu R9800 vacuum tube photomultipliers (grey). The signals from photomultipliers are probed in the voltage domain at four thresholds with the timing accuracy of about 30 ps [58]. The data acquisition system is working in the trigger-less mode [59]. **Right:** Arrangement of the scintillator strips with denoted coordinate system. The strips are oriented along the Z axis.

plastic polymers in place of conventional crystal scintillators was announced in 2009 [60]. Replacing the series of expensive scintillator crystals along the z axis by a single plastic scintillator strip allows to reduce the price of the whole device as well as the complexity of the readout system. This solution enables to build a device from larger scintillators resulting in greater field of view (FOV) and usage of the time of flight (TOF) technique, which significantly improves the resolution of the tomographic image [61]. Commercial TOF-PET systems (developed by GE, Siemens, Philips) have resolution along the line of response (LOR) between 300 and 550 ps, which corresponds to a spatial resolution between 4.5 and 8 cm [61]. The single-strip J-PET prototype shows ability to reach 4.9 cm [62], with the possibility of further improvement by more precise determination of gamma quanta interaction along the strip [63] and by application of other reconstruction methods such as e.g. the compressive sensing theory [64–66]. The J-PET detector was designed as a cost-effective scanner for simultaneous metabolic imaging of the whole human body. However, its superior time resolution, high granularity of detection strips and lower detection pile-ups provide new research opportunities for discrete symmetries violation studies. The detailed J-PET program is described in the Reference [67].

5.1 DESIGN DETAILS

Gamma quanta from e^+e^- annihilation interact with plastic scintillator strips, and cause emission of photons from the visible light spectrum. Usually a few thousand photons are emitted isotropically for 511 keV gamma quanta as a result of the scintillation. The optical signal from the sctintillator is read out at both of its ends by the Hamamatsu R9800 vacuum tube photomultipliers (PMT). In order to decrease photon losses the sides along a scintillator strip are covered with reflective foil. Polymers absorb internally less light emitted by scintillation from radiation than crystals, therefore the usage of longer polymer scintillator strips is possible. The J-PET detector consists of three layers of EJ-230 plastic scintillator strips with dimensions of $7 \times 19 \times 500$ mm^3. The innermost and middle layers consist of 48 strips each, while the outermost layer - 96 strips. Another advantage of the plastic scintillators over commonly used crystals is their lower price and shorter duration of signals (about 5 ns compared to 45 ns for LYSO crystal) [68]. This allows to use high activity sources and fast digital electronics readout [58, 59]. The J-PET Data Acquisition System is build out of Trigger Readout Board v3 hardware equipped with Time-to-Digital Converters (TDC) and Field Programmable Gate Array devices for the TDC readout and data transmission. Each analog signal from the PMT is sampled in the voltage domain at four thresholds. This gives 4 points on the leading edge and 4 points at the trailing edge of the signal. A scheme of the registration process is shown in Figure 5.2. Probing signals at four thresholds

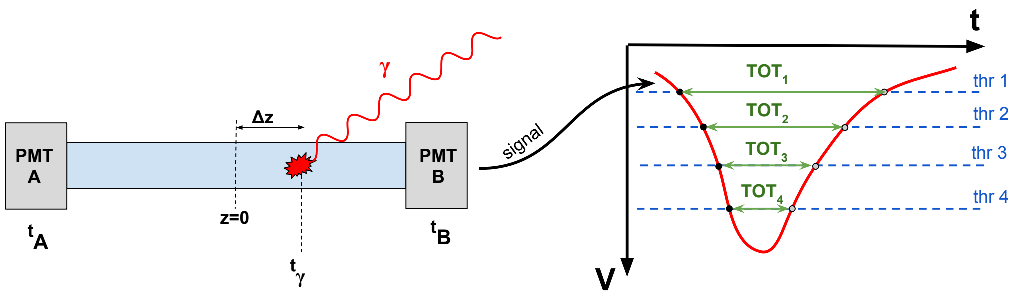

Figure 5.2: **Left:** Incident gamma quantum (red) interacts with detector strip and causes the emission of photons, later registered by a photomultipliers (PMT). **Right:** Recorded signal is sampled at four voltage threshold levels (blue lines). Each signal crossing a given threshold is registered at both leading and trailing edge (black and grey dots respectively). Recorded times at both PMT's (t_A and t_B) are used for determination the gamma quantum interaction place and time (t_γ) along the scintillator strip (see Eq. 5.2 and 5.1). The value of deposited energy corresponds to the sum of registered times over threshold (TOT) for all thresholds crossed by the signal.

allows to reconstruct the original signal shape [66]. Data is collected continuously (in a trigger-less mode) to ensure that the registered information is preserved and stored for further, high-level processing preformed by dedicated analysis software described in Section 5.3.

5.2 J-PET DETECTOR PROPERTIES

The time and position of a gamma quantum interaction (referred to as a hit further in the text) in a scintillator can be calculated from the time of scintillation light registration in photomultipliers located at the ends of a single plastic scintillator strip (t_A, t_B). The distance (Δz) along the strip between its center and the hit position (see Figure 5.2, left) can be expressed as:

$$\Delta z = \frac{(t_A - t_B) \cdot v}{2}, \tag{5.1}$$

where v is the effective light signal velocity in the plastic scintillator [69]. The time of interaction t_γ is obtained from a sum of the light registration times at sides A and B of the scintillator:

$$t_\gamma = \frac{t_A + t_B}{2} - \frac{L}{2v}, \tag{5.2}$$

where L is the length of scintillator strip.

Gamma quanta interact with polymer scintillators mainly via the Compton effect and the characteristic spectra of deposited energy are described with a differential cross section for scattering in a solid angle $d\Omega$ given by the Klein-Nishina formula [70]:

$$\frac{d\sigma}{d\Omega} = \frac{r_0^2}{2}\left(\frac{E'}{E}\right)^2\left[\frac{E'}{E} + \frac{E}{E'} - \sin^2\phi\right], \tag{5.3}$$

where r_0 is the classical electron radius, E and E' denote energies of the primary and scattered photon and ϕ is the planar angle between their momenta.

The J-PET detector measures the deposited energy using time over threshold (TOT) [71]. The TOT value for a single threshold is determined based on registered times on leading (t^L) and trailing (t^T) edges of the signal:

$$TOT = t^T - t^L. \tag{5.4}$$

The total energy deposited by gamma quanta is correlated with the sum of TOTs at all thresholds crossed by the signals on both A and B sides of a scintillator.

The obtained energy and time resolution of registered gamma quanta were experimentally determined and within the range of deposited energy E_{dep} which corresponds to $(200, 340)$ keV, are equal to [72]:

$$\sigma(T^0_{hit}) \approx 80 \text{ ps}, \tag{5.5}$$

$$\frac{\sigma(E)}{E} = \frac{0.44}{\sqrt{E\,[\text{MeV}]}}. \tag{5.6}$$

For lower energies the time resolution can be expressed as a function of deposited energy (E_{dep}) [20]:

$$\sigma(T_{hit}(E_{dep})) = \frac{\sigma(T^0_{hit})[\text{ps}]}{\sqrt{\frac{E_{dep}[\text{keV}]}{270}}}. \tag{5.7}$$

Considering the most challenging time reconstruction for gamma quanta with low energies (around 50 keV), one can see that the J-PET detector provides a precision on the level of 200 ps. In the commercial PET systems the events with an energy deposition lower than about 400 keV are discarded [73, 74].

5.3 SOFTWARE ANALYSIS - FRAMEWORK

The J-PET data reconstruction is a multi-stage process based on dedicated analysis software, the J-PET Analysis Framework [75]. It is developed in a C++ programming language and is based on the Open Source library ROOT [76]. The source code of the project is available on the GitHub service [77] under the Apache Licence.

The analysis of data with the J-PET Framework consists of several modules. Each of them corresponds to a particular computing task e.g. calibration procedure or reconstruction algorithm. This approach allows the user to choose between available reconstruction algorithms or create a dedicated analysis module and easily implement it into the data processing chain. A scheme of the flow of data delivered by the data acquisition system (DAQ) is shown in Figure 5.3.

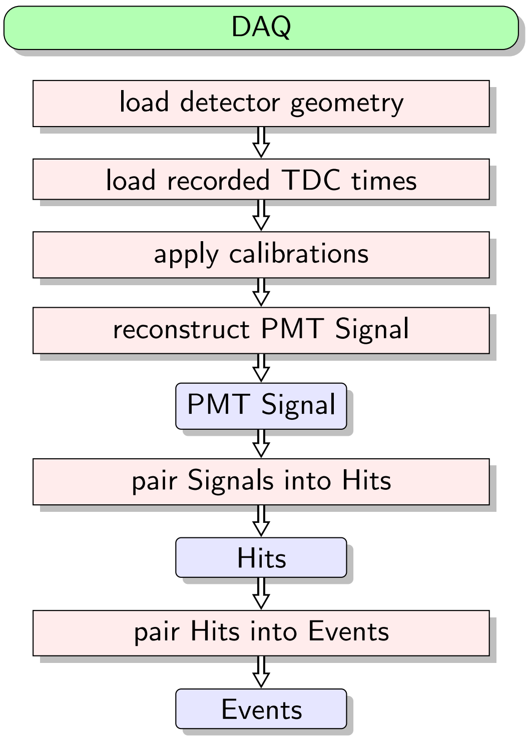

Figure 5.3: Scheme of data processing by the J-PET Analysis Framework software. The input data (recorded TDC times) are delivered by data acquisition system (DAQ). Pink rectangles represent computational task responsible for e.g. calibration or a reconstruction algorithm. Violet rectangles stand for reconstructed physical quantities e.g. gamma interaction points in the scintillator strip (referred as hits). The TDC signals are used to reconstruct shapes of electric signals from photomultipliers. Next, pairs of signals from a single photon hit in a scintillator strip allow for reconstruction of the hit time and position along the strip. Finally, hits identified to originate from a single annihilation event are merged into event structures.

6 PERFORMANCE ASSESSMENT: MONTE CARLO SIMULATION

Part of the presented work was to develop the Monte Carlo simulation package of the J-PET detector. The program is based on the Geant4 simulation package [78], which controls the tracking of particles through detector geometry and uses well tested routines to simulate interactions.

In the further section, an integration of the output from the developed simulation program with the existing J-PET analysis software will also be presented. The preformed simulation results in an estimation of the accuracy of $\mathcal{CPT}$ violation parameters as a function of the number of registered o-Ps→ 3γ decays.

6.1 PROGRAM ARCHITECTURE AND SIMULATED GEOMETRY

The core of the Monte Carlo simulation is conducted by the Geant 4 simulation software [78], while the detector description and details on the o-Ps→ 3γ annihilation process (not included in Geant4 physics) are implemented as a part of this dissertation. Code is available under an Apache Licence on the GitHub service [79].

From the user point of view, the files containing MC-generated events have to be processed in the same manner as collected data (see section 5.3). For this purpose a dedicated module is created as a part of the J-PET Analysis Framework. As an input it uses structures created by the Geant4 software with generated information about gamma quanta interactions. In further steps of the analysis chain, those hits are processed in the same manner as experimental data. A scheme of the data flow is shown in Figure 6.1. The Monte Carlo simulations account for: angular and energy distributions of gamma quanta originating from direct e^+e^- or ortho-positronium annihilation, Compton interactions of emitted gamma quanta in the detector built from plastic scintillators, determination of gamma quanta hit-position and hit-time in the detector with resolutions known from experiment, multiple scattering and accidental coincidences, as well as reconstruction of registered gamma quanta four-momenta.

Simulations were performed assuming a detector geometry with three cylindrical detection layers that corresponds to the J-PET detector. In addition, the supporting frame was created based on Computer Aided Design (CAD) technical drawings and loaded directly while executing the simulations. An exemplary view of a simulated geometry is shown in Figure 6.2.

6.2 POSITRONIUM FORMATION

An isotope undergoing a β^+ decay emits a positron that travels through matter, scatters and slows down reaching thermal energies. Then it undergoes free annihilation or forms a positronium [80]. In water at $20°$C the positron has about 64% chance of undergoing free annihilation [81]. The positronium is produced mostly in

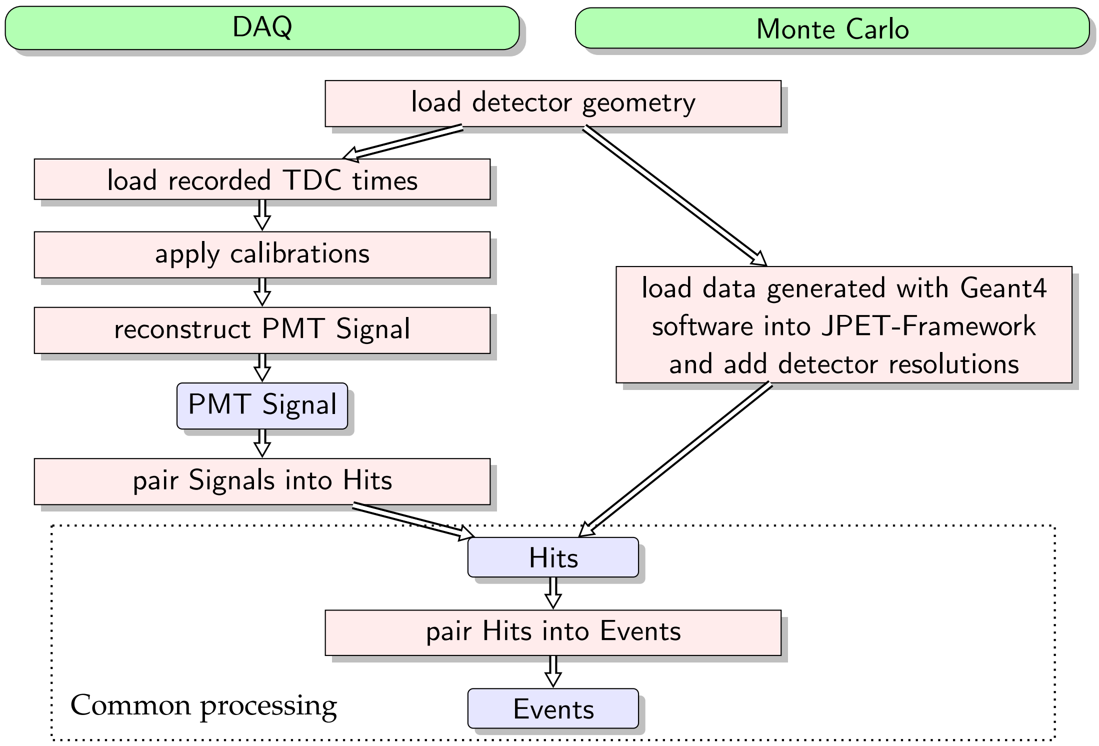

Figure 6.1: Scheme of data processing by the J-PET Framework software with implemented module dedicated for Monte Carlo simulation processing. Left and right columns correspond to the input taken from DAQ or Monte Carlo simulation, respectively. Violet rectangles represent reconstructed physical information obtained from dedicated analysis modules (pink rectangles). Reconstructed hits, both from DAQ system or Monte Carlo simulation, pass in the further steps through the same reconstruction algorithms.

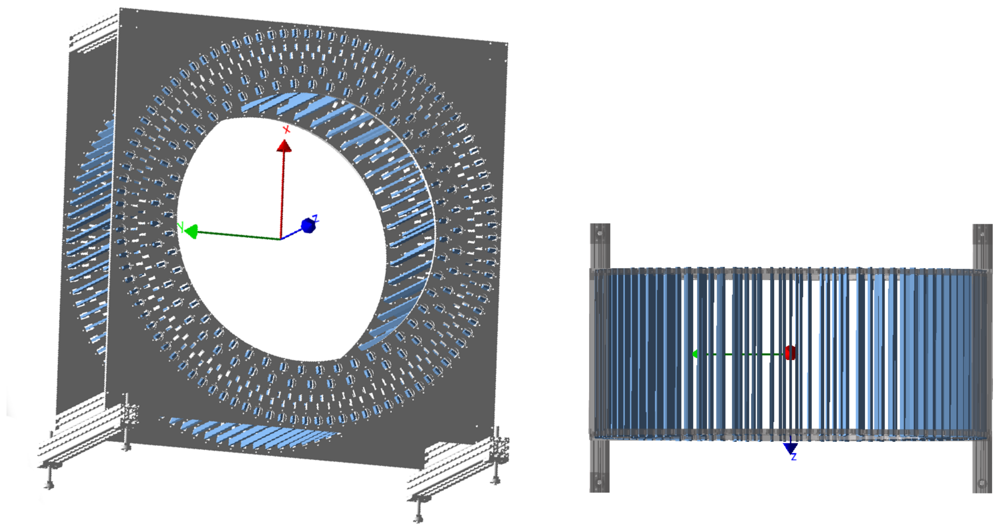

Figure 6.2: Front (left panel) and top (right panel) visualization of simulated detector (to be compared with Figure 5.1). The detection strips (blue) are organized into three cylindrical layers and mounted between two detector frames (grey).

the ground state forming para-Positronium ($^1S_0$, p-Ps) or ortho-positronium ($^3S_0$, o-Ps) with probabilities of 25% and 75%, respectively. The annihilation of these states is leading predominantly to an emission of two or three gamma quanta for p-Ps or o-Ps states, respectively. However, the interactions with matter can lead to inversion of the ortho-positronium spin or to the pick-off processes and, as a result, can affect the relative ratio of $3\gamma/2\gamma$ annihilation. The fraction of atoms annihilating into 3γ quanta is described by following equation [82]:

$$f_{3\gamma} = \frac{1-P}{372} + \frac{3}{4}\frac{\tau_{o-Ps}}{\tau_{vacc}}P, \tag{6.1}$$

where P denotes o-Ps formation probability, τ_{o-Ps} and τ_{vacc} is the o-Ps lifetime in a sample and in vacuum, respectively. The effective yield of annihilation into 3γ in most of non-metallic substances is of the order of 1%, although in some cases, as for example fine powders of alkaline oxides, it can reach even 29% as recently shown for the amberlite porous polymer XAD-4 (CAS 37380-42-0) [83].

6.3 SIMULATION OF BACK-TO-BACK ANNIHILATION EVENTS

In the PET tomography the registration of two gamma quanta from e^+e^- annihilation is essential. Due to momentum conservation they are emitted back-to-back. Annihilation quanta interact with the plastic scintillators used in J-PET. However, usage of plastics scintillators, due to their low density, results in a lower registration probability. Linear absorption coefficient of 511 keV gamma quanta for plastic scintillators amounts to 0.098 cm^{-1} [84], and is more than eight times smaller than for the LSO crystal amounting to 0.821 cm^{-1} [85].

In polymer scintillators, incident gamma quanta are mainly interacting through Compton scattering described by the Klein-Nishina formula [70].

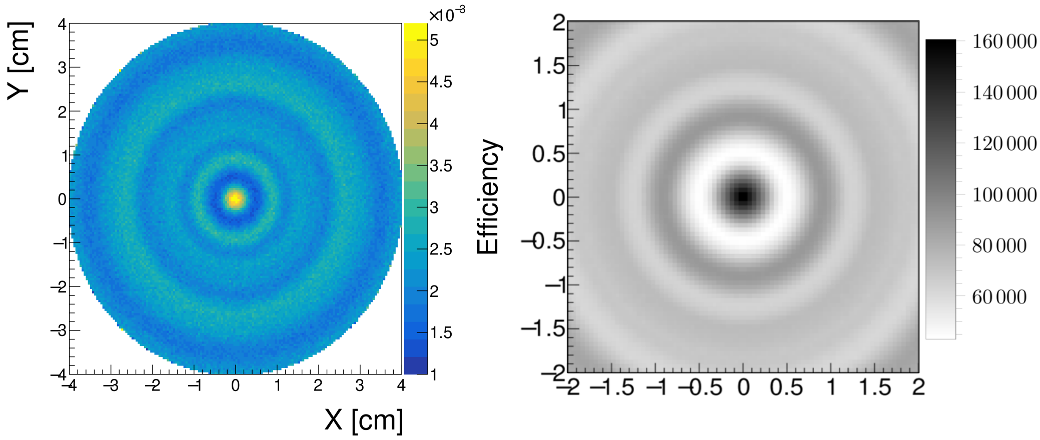

Figure 6.3: **Left:** Registration efficiency for 2 γ quanta originating from direct annihilation. The efficiency map was estimated with 0.5 mm $\times$ 0.5 mm bin size. **Right:** Sensitivity map in X-Y plane in the central part of the detector ($z = 0$). Result obtained as a part of derivation of a statistical model for the J-PET detector necessary for image reconstruction purposes. Right figure adapted from [86]. The spatial configuration of J-PET detector strips and the requirement of two hits registration along the LOR results in characteristic structures visible on the sensitivity map.

Registration of 2γ annihilation events requires reconstruction of signals from two strips. Non-solid detection layers coverage with scintillator strips results in "blind spots" - areas lying inside the detector where registration probability is zero or close to zero and emitted gamma pairs are not detected by any of the scintillator pairs. The J-PET detector configuration of detection strips results in the efficiency map presented in Figure 6.3.

6.4 SIMULATION OF 3γ EVENTS

Positronium is the lightest purely leptonic system, and it can annihilate only into gamma quanta. In case of the decay into three photons, they are coplanar in the Center of Mass (CM) frame due to momentum conservation. The double differential cross section as a function of photons' energies E_1 and E_2 is expressed as [87]:

$$\frac{d^2\sigma}{dE_1 dE_2} = \frac{1}{6}\frac{8e^6}{vm_e^2}\left[\left(\frac{m_e - E_3}{E_1E_2}\right)^2 + \left(\frac{m_e - E_2}{E_1E_3}\right)^2 + \left(\frac{m_e - E_1}{E_2E_3}\right)^2\right], \tag{6.2}$$

where e and m_e are electron charge and mass, respectively, v denotes electron-positron relative velocity, E_i (i=1,2,3) are gamma photon energies, and $E_1 + E_2 + E_3 = 2m_e$ follows from energy conservation. In above formula, the conservation of four-momentum results in the characteristic energy distribution of gamma quanta (see Figures 6.4). Energy of single gamma quanta from ortho-positronium annihilation is within the $[0, 511]$ keV range and the spectrum of deposited energy is presented in Figure 6.5.

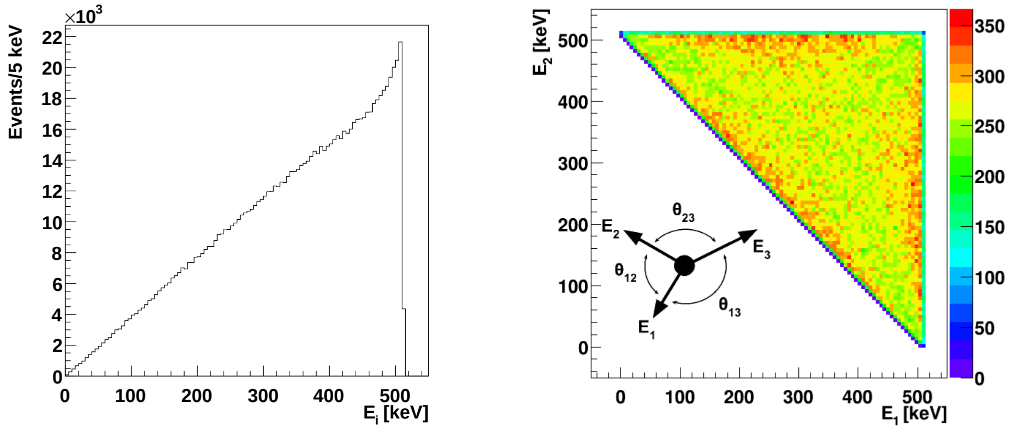

Figure 6.4: Left: Energy spectrum of photons originating from three-photon annihilation of an electron and a positron. Right: Dalitz plot for the o-Ps→ 3γ annihilation. In both figures the non-homogeneity of the density distribution is due to the energy dependence of the o-Ps→ 3γ transition amplitude (see Eq. 6.2) which was taken into account in simulations according to the predictions based on quantum electrodynamics [87].

The registration efficiency of the photons from the o-Ps→ 3γ events depends on the energy deposition threshold used in the front-end electronics. The hardware threshold at the order of 10 keV [72] is set to discriminate the experimental noise and further selection threshold based on the measured energy deposition is applied. The probability of registration of 1, 2 or 3 gamma quanta originating from o-Ps→ 3γ annihilation as a function of applied selection threshold is shown in Figure 6.6 (right panel). The left panel shows the efficiency map in the $X - Y$ plane in the center of detector. The o-Ps→ 3γ is a three-body annihilation, therefore the observed efficiency map has a uniform distribution.

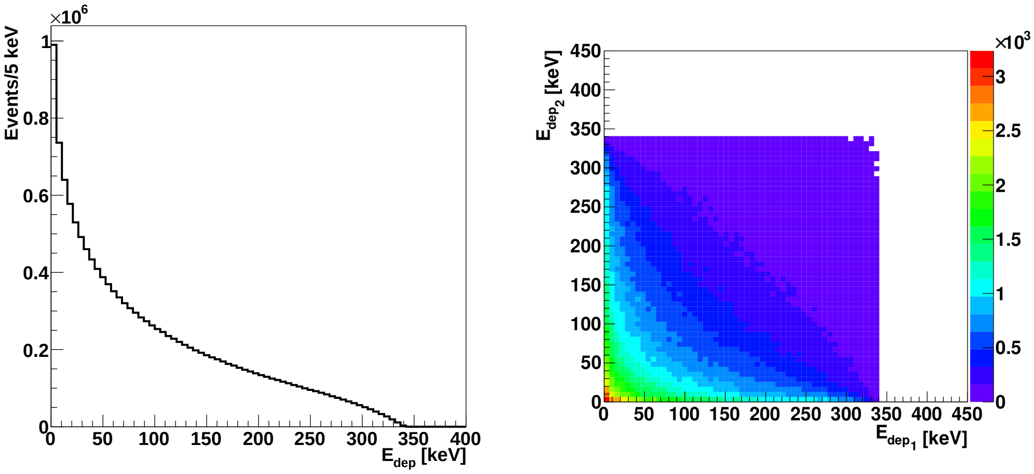

Figure 6.5: Distribution of energy deposited in plastic scintillators by gamma quanta originating from o-Ps→ 3γ annihilations for single gamma quanta (left panel) and for two gamma quanta randomly selected (right panel). The shown spectrum is a convolution of the energy distribution of gamma quanta from the o-Ps→ 3γ decay (Figure 6.4, left panel) and the Klein-Nishina distribution of kinetic energy of electrons acquired via Compton scattering.

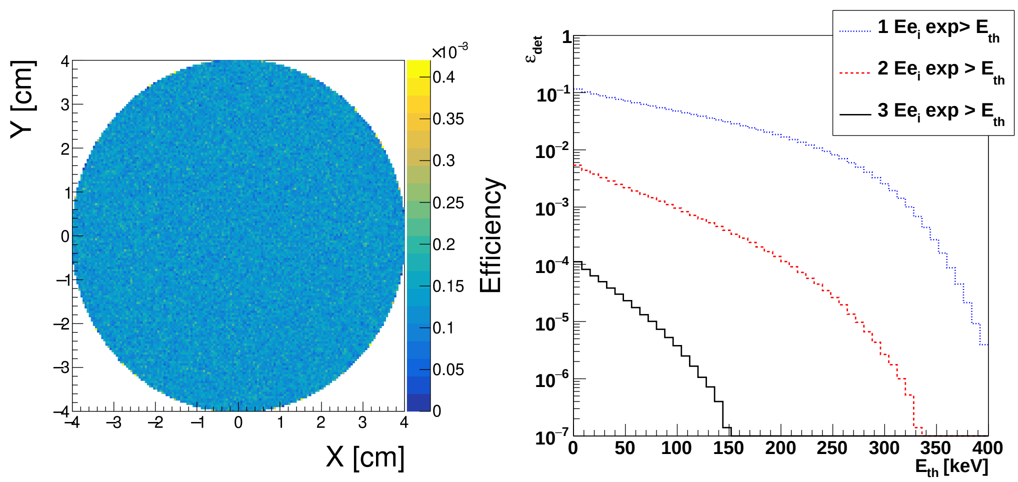

Figure 6.6: The o-Ps→ 3γ registration efficiency (determined taking into account geometrical acceptance, probability of gamma quanta registration in the plastic scintillator and J-PET detector resolution) for transverse view of a central plane of the detector (left panel) and as a function of the applied threshold (right panel). The shown dotted, dashed and solid lines indicate efficiency assuming that at least one, two or three photons deposited energy above the threshold, respectively. While reconstruction of o-Ps→ 3γ events requires low experimental threshold, its efficiency map is free of the blind spots which results from detector arrangements in case of 2γ back to back reconstruction (compare Figure 6.3)

7 FEASIBILITY STUDY

Recent studies on $\mathcal{CPT}$ odd triple correlations $\vec{s} \cdot \left(\vec{k}_1 \times \vec{k}_2\right)$, where $\vec{s}$ is the spin of the ortho-positronium, and $\vec{k}_1$ and $\vec{k}_2$ are the momenta of the two most energetic annihilation photons, were suggested in [16] and performed by Vetter and Freedman using the Gammasphere detector [17].

Gammasphere is an array consisting of 110 high purity germanium (HPGe) detectors. Each Ge detector assembly consists of a 7 cm diameter and 8 cm long cylindrical HPGe detector surrounded by six bismuth germanate (BGO) scintillators on the sides and one BGO scintillator in the back [88]. The probability that a detected 511 keV photon deposits its full energy is roughly 15%.

In the experiment with Gammasphere, the 0.37 MBq source of ^{68}Ge or ^{22}Na was placed underneath a thin (0.2 mm) plastic scintillator and a hemisphere of silicon dioxide aerogel. Positrons from β decay were identified by around 70 keV energy deposition in the scintillator. The average ortho-positronium polarization $\langle P \rangle$ was 21.5% for ^{22}Na and 30.5% for ^{68}Ge. The magnitude of the source polarization is reduced by accepting positrons in a solid angle of 2π. During the 36 day run, the Gammasphere reconstructed around 2.65×10^7 o-Ps$\rightarrow 3\gamma$ annihilation events [17].

The observable measured by the Gammasphere was the asymmetry:

$$A = \frac{N_+ - N_-}{N_+ + N_-}, \tag{7.1}$$

where N_+ and N_- denote number of decays with the normal to the decay plane parallel (+) and antiparallel (-) to the o-Ps spin direction, respectively (see Figure 1.2). The angular correlation between spin and decay plane is related to the count asymmetry observed in the experiment and the average polarization of the o-Ps $\langle P \rangle$, by [17]:

$$C_{CPT} = A/\left\langle P \right\rangle = 0.0026 \pm 0.0031. \tag{7.2}$$

The obtained result is the most precise measurement to date.

The rate limitation of the previous experiment can be overcome by the J-PET detector due to its much higher granularity and about one to two orders of magnitude shorter duration of signals (plastic scintillators at the J-PET [68, 72] vs. HPGe/BGO at Gammasphere [17]) leading to significant reduction of pile-ups. It is also important to stress that the J-PET detector is characterized by about 3 times higher angular resolution and time resolution (~ 0.1ns) [68, 72] is improved by about a factor of ten with respect to the Gammasphere detector [17]. An improvement on the precision of $\mathcal{CPT}$ symmetry violation test is also expected because of about two orders of magnitude larger statistics, which can be achieved due to the possibility of longer runs and due to the usage of the higher activity of positron source (10 MBq at the J-PET vs. 0.37 MBq at Gammasphere [17]).

7.1 POLARIZATION CONTROL

During past experiments, the ortho-positronium decay point was assumed to lie within the aerogel targets, e.g. hemisphere in Gammasphere, and its exact time and spatial coordinates were not reconstructed. In J-PET, however, due to its relatively high angular acceptance and timing resolution, a reconstruction of the o-Ps$\rightarrow 3\gamma$ process is possible by means of a new trilateration-based reconstruction method. The algorithm was developed and tested, and obtained results are presented in References [89] and [90].

The method based on trilateration allows for a simultaneous reconstruction of both location and time of the annihilation based on time and interaction position of gamma quanta in the J-PET detector. Gamma quanta from the o-Ps$\rightarrow 3\gamma$ annihilation travel on a distance between the annihilation point (which needs to be localized) and the detector where the places and times of their interaction are recorded and serve as reference points. An additional constraint is given by the fact that all three photons are produced in a three-body decay and thus their momenta as well as the o-Ps decay point are contained within a single plane in the frame of reference of the decaying positronium atom.

Experimental realization of triple correlation measurements $\vec{s} \cdot \left(\vec{k}_1 \times \vec{k}_2\right)$ requires a vacuum chamber whose walls are coated on the inner side with a porous medium for o-Ps production (see Figure 7.1). In the center of the chamber a β^+ source is

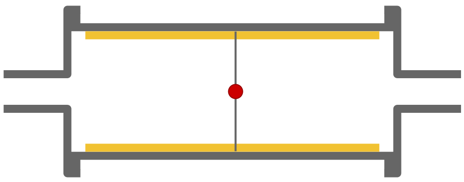

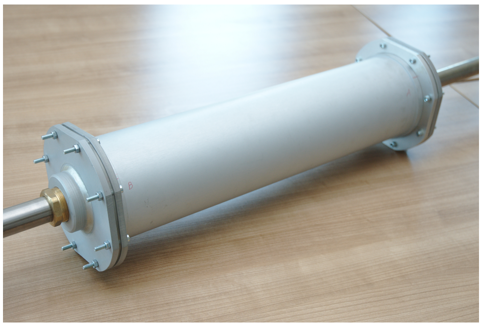

Figure 7.1: **Left:** Longitudinal cross-section of an ortho-positronium annihilation chamber (grey) allowing for o-Ps spin direction determination. The radioactive source is located in the center (red dot) and ortho-positronium is formed in porous material (yellow). **Right:** Annihilation chamber prototype.

located, and emitted positrons from β^+ decay are polarized along their momentum with $\vec{P} = \vec{v}/c$, where the $\vec{v}$ and c denotes positrons velocity and speed of light, respectively. The average polarization can be estimated from the average velocity of the positrons emitted in the β^+ decays. If positrons are emitted in a cone with an opening angle of 2α, then the aforementioned equation can be expressed as:

$$\langle P \rangle = \frac{v}{c} \left(1 + \cos\alpha\right)/2. \tag{7.3}$$

The polarization of the ortho-positronium is (from a statistical argument) simply 2/3 of the average positron polarization [33].

The capability of reconstruction of ortho-positronium annihilation coordinates allows for a more precise polarization estimation, presented schematically in Figure 7.2.

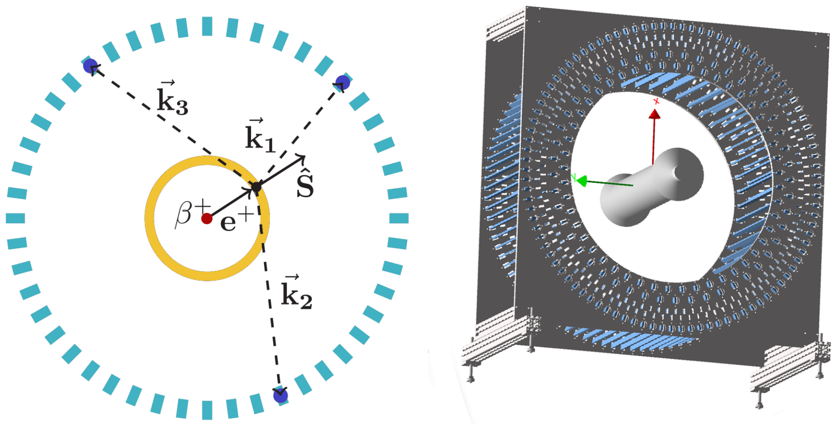

Figure 7.2: **Left:** Illustration of ortho-positronium spin determination. In the center of the detector a β^+ source is located (red dot), and the emitted positron may form an ortho-positronium state in the aerogel (yellow band). Dashed lines represent gamma quanta originating from ortho-positronium annihilation. Emitted gamma quanta are registered by scintillator strips represented by the circularly arranged blue squares. Based on registered hits positions and times, the annihilation vertex is reconstructed on the cylinder, which, in turn, allows to estimate the positron momentum direction and ortho-positronium spin direction. Figure adapted from [89]. **Right:** Visualization of the detector with an annihilation chamber placed at its center.

With the J-PET detector and the cylindrical positronium target with a radius of 10 cm the uncertainty of determination of positron direction will amount to about 15° [89]. In a conducted test measurement a large annihilation chamber and 9 MBq sodium source were used. The source was closed in the Kapton foil inside the cylindrical aluminum chamber. In the first tests, positrons were annihilating in the aluminum wall [90]. In the next experiments, the annihilation chamber will be realized as the positron source with a porous material cylinder around it, where we plan to use porous target materials like polymer XAD-4 (CAS 37380-42-0) [83] on the internal surfaces of the chamber.

7.2 BACKGROUND REDUCTION

Annihilation into 2γ may mimic a registration of 3γ annihilation due to the secondary scatterings in the detector. Such scattering is shown pictorially in Figure 7.3. For the reduction of this background the following complementary methods can be considered, based on information of:

- relation between position of the individual detectors which recorded hits and the time difference between registered hits,
- angular correlation of relative angles between the gamma quanta propagation directions,
- the distance between the origin of the annihilation (position of the annihilation chamber) and the decay plane.

In Figure 7.4 example spectra of θ_{23} vs θ_{12} distribution are shown, where θ_{ij} are the opening angles order that $\theta_{12} < \theta_{23} < \theta_{13}$ (see Figure 7.3) between registered

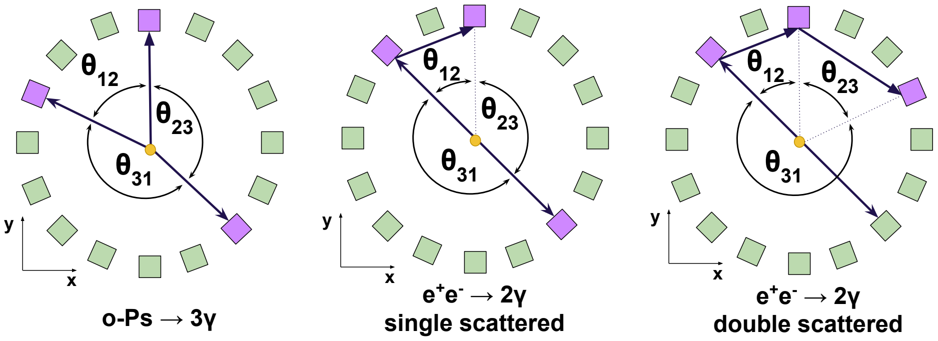

Figure 7.3: Pictorial illustration of the possible response of the detector to o-Ps→ 3γ and e^+e^- annihilation into 2γ. Circularly arranged squares represent scintillator strips - purple and green colors indicate strips where the gamma quanta were or were not registered, respectively. For clarity, the elements are shown not to scale. Only a single layer with selected number of scintillators and increased $X-Y$ dimensions is shown. The arrows represent the actual gamma quanta occurring in the events, while dotted lines indicate naively reconstructed gamma quanta. Examples of primary and secondary scatterings are depicted.

gamma quanta. For the o-Ps→ 3γ process, due to the momentum conservation, $\theta_{23} > 180° - \theta_{12}$ and therefore events corresponding to the o-Ps→ 3γ decay will lie above the diagonal, as shown in green colour in Figure 7.4.

Most of the background events will correspond to points at the diagonal ($\theta_{23} = 180° - \theta_{12}$) and below diagonal ($\theta_{23} < 180° - \theta_{12}$) as can be inferred from the middle and left panel of Figure 7.3. Therefore, one of the possible selection cuts was applied on ordered opening angles ($\theta_{12} < \theta_{23} < \theta_{13}$) between registered gammas, and resulted in a decrease of background by a factor 10^4 while rejecting only 3% of signal events (see Figure 7.4). Combining aforementioned criterion with the requirement that registered time difference (Δt) as a function of the difference between sequential numbers of the detectors (ΔID) is small ($\Delta t < 0.3$ ns) allows for total reduction of the instrumental background by a factor of 10^9. Therefore, even though the 3γ events are expected to constitute only about 0.5 % of 2γ events, the background due to the 2γ annihilation associated with a secondary scattering in the detector can be reduced to a negligible level.

However, we have to take into account that the remaining background is caused not only by misidentified 2γ events, but also by true annihilations into 3γ which may originate from the interaction of the positronium with surrounding electrons and hence will constitute a background for studies of discrete symmetries. Interaction of ortho-positronium with matter is classified into: pick-off annihilations and ortho-para spin conversion. Contribution from these processes depends on the used target material, e.g. in aerogel IC3100 and amberlite porous polymer XAD-4 about 7% and 36% of ortho-positronium undergo these interactions, respectively [83]. The events originating from the true o-Ps→ 3γ annihilation process (N_{o-Ps}) can be misidentified with the events from the following processes: pick-off process with direct annihilation to 3γ ($N_{3\gamma\ pick-off}$); pick-off process with annihilation to 2γ misidentified as 3γ due to secondary scatterings ($N_{2\gamma\ pick-off}$); conversion of ortho-positronium to para-positronium with subsequent C symmetry violating decay to 3γ ($N_{3\gamma\ conv}$); conversion of ortho-positronium to para-positronium with

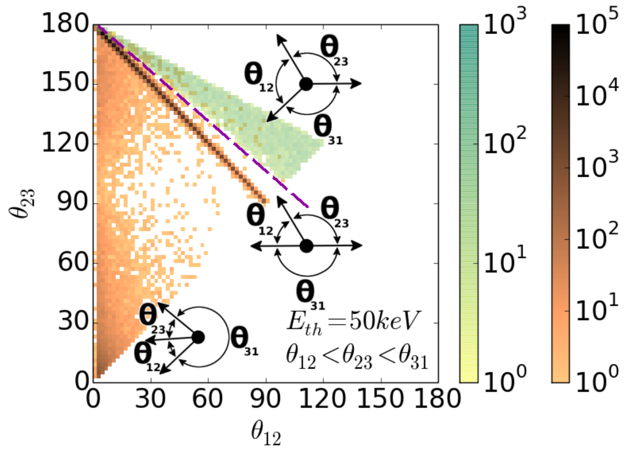

Figure 7.4: Monte Carlo distribution of o-Ps→ 3γ (green) and scattered events (brown) as a function of θ_{12} vs θ_{23} angles. Events, where one of the gamma from $e^+e^- \to 2\gamma$ annihilation is registered in the detector while the other is scattered and cause signals in two detectors, lie on the diagonal of the plot. Events where one gamma is missing detection, and the other undergoes two scatterings are localized below the diagonal line. Example of an analysis cut, rejecting 3% of signal and reducing background by factor 10^4 is shown as a dashed purple line. The presented distribution includes the angular resolution of the J-PET detector.

subsequent annihilation to 2γ misidentified as 3γ due to the secondary scatterings ($N_{2\gamma\ conv}$).

The conservative upper limit on these background contributions may be estimated as:

$$\frac{N_{2\gamma\ conv}}{N_{o-Ps}} < \frac{N_{2\gamma\ pick-off}}{N_{o-Ps}} < \frac{N_{3\gamma\ conv}}{N_{o-Ps}} < \frac{N_{3\gamma\ pick-off}}{N_{o-Ps}}, \tag{7.4}$$

where:

$$\begin{aligned}
\frac{N_{3\gamma\ pick-off}}{N_{o-Ps}} &< \left(1 - \frac{\tau_{matter}}{\tau_{vacuum}}\right)/370 \approx 2 \cdot 10^{-4}(\text{IC3100}) < 10^{-3}(\text{XAD-4}); \\
\frac{N_{2\gamma\ pick-off}}{N_{o-Ps}} &< 0.07 \cdot 10^{-9}(\text{IC3100}) < 0.36 \cdot 10^{-9}(\text{XAD-4}); \\
\frac{N_{3\gamma\ conv}}{N_{o-Ps}} &< 0.07 \times 2.8 \cdot 10^{-6}(\text{IC3100}) < 0.36 \times 2.8 \cdot 10^{-6}(\text{XAD-4}); \\
\frac{N_{2\gamma\ conv}}{N_{o-Ps}} &< 0.07 \cdot 10^{-9}(\text{IC3100}) < 0.36 \cdot 10^{-9}(\text{XAD-4}).
\end{aligned} \tag{7.5}$$

In the above estimations the factor 10^{-9} denotes the reduction power of the 2γ events and $2.8 \cdot 10^{-6}$ stands for the upper limit on the C symmetry violation via the p-Ps $\to 3\gamma$ process [91]. The precise control of these contributions will be provided by the measurement of the true 2γ events with high statistics.

7.3 J-PET EFFICIENCY STUDIES WITH MONTE CARLO SIMULATIONS

The rate of registered o-Ps→ 3γ events in general can be expressed by the formula:

$$R_{o-Ps\to 3\gamma} = A \cdot f_{o-Ps\to 3\gamma} \cdot \epsilon_{det}(th) \cdot \epsilon_{ana}, \tag{7.6}$$

where A is the total annihilation rate (fast timing of applied plastic scintillators allows for usage of a 10 MBq positron source), $f_{o-Ps\to 3\gamma}$ is the fraction of annihilations via o-Ps→ 3γ process in the target material, $\epsilon_{det}(th)$ is the detector efficiency as a function of applied detection threshold while ϵ_{ana} denotes selection efficiency used to discriminate between 3γ and 2γ events.

The ϵ_{det} efficiency of the o-Ps→ 3γ reconstruction will depend on the energy deposition threshold used in the analysis. The probability of registration of 1, 2 or 3 gamma quanta originating from o-Ps→ 3γ annihilation (ϵ_{det}) as a function of the applied selection threshold is shown in Figure 6.6 (right panel). The efficiency ϵ_{det} contains contribution from geometrical acceptance, probabilities of gamma quanta interaction in the plastic scintillators used and it was determined taking into account the J-PET detector resolution. In evaluation of ϵ_{det}, it is assumed that the event selection threshold is set to 50 keV. A fraction of annihilations via o-Ps→ 3γ process is estimated taking into account only the longest lived component in two selected materials IC3100 ($f_{o-Ps\to 3\gamma} = 16.6\%$) and XAD-4 ($f_{o-Ps\to 3\gamma} = 28.6\%$) [83]. The expected rate of registered signal events per second is 15 for IC3100 and 25 for XAD-4. Using amberlite porous polymer XAD-4 instead of aerogel IC3100 as target material in the experiment, allows to collect the required statistics almost twice faster, however, resulting in higher systematic uncertainties due to the interaction of positronium with the target material, as discussed in Section 7.2.

7.4 DISCUSSION AND PROSPECTS

The $\mathcal{CPT}$ violating parameter uncertainty depends on the number of reconstructed o-Ps annihilations and spin measurement accuracy. This dependency for the Gammasphere detector is shown in Figure 7.5.

Based on the preformed Monte Carlo simulations it was concluded that the J-PET multipurpose detector constructed at the Jagiellonian University allows for exclusive registration of the decays of ortho-positronium into three photons (o-Ps→ 3γ). Using XAD-4 as the target material, the 10^9 o-Ps→ 3γ events will be reconstructed after 15 months of continuous data taking. This time can be reduced to 50 days by adding two additional layers of scintillation strips [20]. The achieved results indicate that the J-PET detector gives a realistic chance to improve the best present limits established for the $\mathcal{CPT}$ symmetry violation in the decays of positronium [17] by more than an order of magnitude. This can be achieved by (i) collecting at least two orders of magnitude higher statistics, due to the possibility of using a β^+ source with higher rate (10 MBq at J-PET vs 0.37 MBq at Gammasphere [17] experiment), (ii) the enhanced fraction of 3γ events by the use of the amberlite polymer XAD-4, (iii) measurements with a few times improved angular resolution and (iv) about two times higher degree of o-Ps polarization, as shown recently in Reference [89]. The limitation on the source activity can be overcome by the J-PET detector due to the application of plastic scintillators that

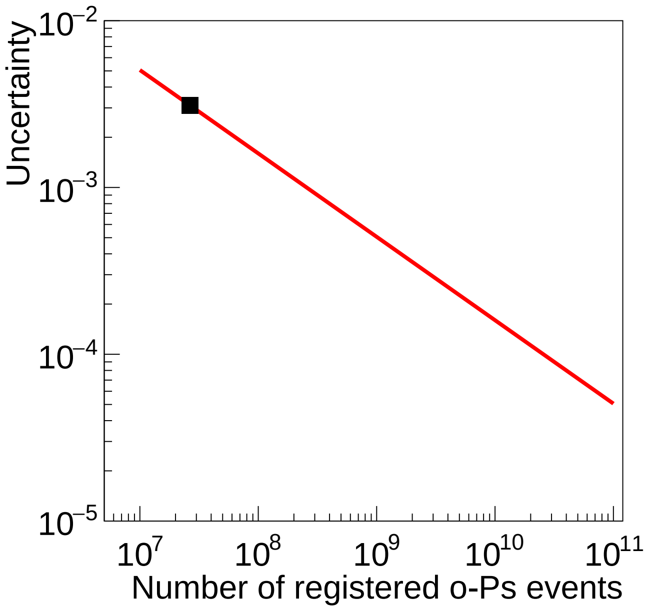

Figure 7.5: Dependency between the number of reconstructed o-Ps→ 3γ events and the uncertainty of $\mathcal{CPT}$ violating parameter (red line). Plot is made assuming that uncertainty on the asymmetry goes as the inverse of the square root of the total number of events and that detector and analysis parameters follow the Gammashpere. Result obtained by Vetter and Freedman [17] is denoted by black square.

are characterized by about two orders of magnitude shorter duration of signals, thus decreasing significantly the pile-up problems with respect to the crystal based detector systems. In addition, the improved angular resolution combined with the superior timing of the J-PET detector (improved by more than order of magnitude with respect to the crystal detectors) and with the possibility of the triggerless registrations [59] of all kind of events with no hardware coincidence window allow for suppression and monitoring of the background due to misidentification of 2γ events and possible contribution from 3γ pick-off annihilations.

8 CONCLUSIONS

The aim of this thesis was to investigate the $\mathcal{CPT}$ symmetry violation effects in two matter-antimatter systems created by different fundamental components: quark-antiquark and lepton-antilepton.

In the first part, a neutral kaon system, formed from combination of $d\bar{s}$ and $\bar{d}s$ quarks, was used to determine the lepton charge asymmetry value for the short-lived kaon. The difference between A_S and the corresponding asymmetry for its long-lived counterpart is sensitive to the $\mathcal{CPT}$ symmetry violation effects. The uncertainty of the test preformed until now was limited by the A_S uncertainty originating mainly from the size of the data sample.

Studies presented in this thesis were conducted on data gathered by the KLOE detector in 2004-2005, and the obtained result:

$$A_S = (-4.9 \pm 5.7_{stat} \pm 2.6_{syst}) \times 10^{-3}, \tag{8.1}$$

improved on the accuracy of the most precise result by a factor of almost two. The combination of the results obtained by the KLOE collaboration gave:

$$A_S = (-3.8 \pm 5.0_{stat} \pm 2.6_{syst}) \times 10^{-3}, \tag{8.2}$$

and allowed to determine new limits on $\mathcal{CPT}$ violating parameters:

$$Re(x_-) = (-2.0 \pm 1.4) \times 10^{-3}, \tag{8.3}$$

$$Re(y) = (1.7 \pm 1.4) \times 10^{-3}, \tag{8.4}$$

which are in agreement with $\mathcal{CPT}$ invariance within the achieved precision.

It is worth mentioning that the data taking campaign has been restarted in 2014 and until march 2018 the KLOE-2 detector collected an additional dataset with an integrated luminosity of 5.5 fb^{-1}. KLOE-2 provides not only larger statistics but also improved event reconstruction due to the new Inner Tracker detector. The detector aims at improving the tracking and vertexing resolution close to the $K_S \to \pi e \nu$ decay point [92].

Another part of the KLOE-2 program is a test of $\mathcal{CPT}$ symmetry in transitions. The difference between the semileptonic asymmetries for K_S and K_L is also accessible while measuring the double ratio of $\mathcal{CPT}$-violating ratios [93]. Analysis details are presented in Reference [90].

In the second part of this thesis, a feasibility study of using the J-PET detector to test the $\mathcal{CPT}$ violation manifested as a non-vanishing angular correlation of photons' momenta was carried out. For this purpose a dedicated Monte Carlo simulation was created. Special emphasis was put on describing the ortho-positronium annihilation into three gamma quanta and the response of the J-PET tomograph. The efficiency maps of the central region of the J-PET detector were determined for two and three gamma quanta annihilations. The conducted studies allowed to determine the radius of the cylindrical aluminium chamber which maximizes the $3\gamma/2\gamma$ ratio. Additionally, the expected measurement time to improve presently most precise result [17] was determined for the currently tested experimental setup, which uses the XAD-4 target material in the cylindrical annihilation chamber.

The expected $\mathcal{CPT}$ violation effects are highly model dependent and no single theory predicting them is known. Therefore, searches for $\mathcal{CPT}$ violations have to be conducted through a broad range of systems. In this thesis more precise limitations were given on parameters $Re(x_{-})$ and $Re(y)$ in the neutral kaon system, and a possible search in the decay of ortho-positronium atoms was discussed. Further results in this field are anticipated, among others, in neutrino oscillations [94] and atomic physics experiments [95].

BIBLIOGRAPHY

1. Noether, A. E. Invariante Variationsprobleme. *Nachr. d. onig. Gesellsch. d. Wiss. zu ottingen, Math-phys. Klasse.,* 235–257 (1918).
2. Lüders, G. Proof of the TCP theorem. *Annals of Physics* **2,** 1–15 (1957).
3. Greaves, H. & Thomas, T. On the CPT theorem. *Studies in History and Philosophy of Science Part B: Studies in History and Philosophy of Modern Physics* **45,** 46–65 (2014).
4. Greenberg, O. W. Why is CPT fundamental? *Foundations of Physics* **36,** 1535–1553 (2006).
5. Mavromatos, N. CPT violation: Theory and phenomenology. *Proceedings, International Conference on Exotic Atoms and Related Topics (EXA 2005): Vienna, Austria, February 21-25, 2005,* 361–372 (2005).
6. Greenberg, O. W. CPT violation implies violation of Lorentz invariance. *Phys. Rev. Lett.* **89,** 231602–231612 (2002).
7. Kostelecky, V. A. & Russell, N. Data Tables for Lorentz and CPT Violation. *Rev. Mod. Phys.* **83.** [updates: arXiv:0801.0287], 11–31 (2011).
8. Ellis, J., Mavromatos, N. E. & Sarkar, S. Environmental CPT Violation in an Expanding Universe in String Theory. *Phys. Lett. B* **725,** 407–411 (2013).
9. Pasquinucci, A. & Roland, K. String theory and the CPT theorem on the world-sheet. *Nucl. Phys.* **B485.** [Erratum: Nucl. Phys.B494,486(1997)], 241–274 (1997).
10. Sakharov, A. D. Violation of CP Invariance, c Asymmetry, and Baryon Asymmetry of the Universe. *Pisma Zh. Eksp. Teor. Fiz.* **5,** 32–35 (1967).
11. Bertolami, O., Colladay, D., Kostelecky, V. A. & Potting, R. CPT violation and baryogenesis. *Phys. Lett. B* **395,** 178–183 (1997).
12. Maiani, L., Pancheri, G. & Pavr, N. *The Second DAΦNE Physics Handbook* (Istituto nazionale di fisica nucleare. Laboratori nazionali di Frascati, 1995).
13. Abouzaid, E. *et al.* Precise Measurements of Direct CP Violation, CPT Symmetry, and Other Parameters in the Neutral Kaon System. *Phys. Rev.* **D83,** 092001–092029 (2011).
14. Ambrosino, F. *et al.* Study of the branching ratio and charge asymmetry for the decay $K(s) \to \pi e \nu$ with the KLOE detector. *Phys. Lett. B* **636,** 173–182 (2006).
15. Harpen, M. D. Positronium: Review of symmetry, conserved quantities and decay for the radiological physicist. *Med. Phys.* **31,** 57–61 (2004).
16. Bernreuther, W., Low, U., Ma, J. P. & Nachtmann, O. How to Test CP, T and CPT Invariance in the Three Photon Decay of Polarized s Wave Triplet Positronium. *Z. Phys.* **C41,** 143 (1988).
17. Vetter, P. A. & Freedman, S. J. Search for CPT-Odd Decays of Positronium. *Phys. Rev. Lett.* **91,** 263401–263405 (2003).

18. Anastasi, A., ..., Kisielewska-Kamińska, D., *et al.* Measurement of the charge asymmetry for the $K_S \to \pi e \nu$ decay and test of CPT symmetry with the KLOE detector. *JHEP*, 21–36 (2018).

19. Kamińska, D. K_S Semileptonic Decays and Test of CPT Symmetry with the KLOE Detector. *Acta Phys. Polon. B* **46,** 19–24 (2015).

20. Kamińska, D. *et al.* A feasibility study of ortho-positronium decays measurement with the J-PET scanner based on plastic scintillators. *Eur. Phys. J.* **C76,** 445–459 (2016).

21. Kamińska, D. *et al.* Searches for discrete symmetries violation in ortho-positronium decay using the J-PET detector. *Nukleonika* **60,** 729–732 (2015).

22. Kamińska, D. Study of K_S semileptonic decays and CPT test with the KLOE detector. *J. Phys. Conf. Ser.* **631,** 012042 (2015).

23. Kamińska, D. Status of the measurement of $K_S \to \pi e \nu$ branching ratio and lepton charge asymmetry with the KLOE detector. *EPJ Web Conf.* **81,** 02007–02010 (2014).

24. Kamińska, D. *Status of measurement of $K_S \to \pi e \nu$ branching ratio and lepton charge asymmetry with the KLOE detector* in *Proceedings, 4th Young Researchers Workshop: Physics Challenges in the LHC Era: Frascati, Rome, Italy, May 12-15, 2014* (2015), 32–38.

25. Kamińska, D. Latest discrete symmetries and Quantum Mechanics studies with KLOE-2. *J. Phys. Conf. Ser.* **800,** 012011–012018 (2017).

26. Gajos, A., Czerwinski, E., Kaminska, D. & Moskal, P. *Patent* PCT/PL2015/05003 (2015).

27. Moskal, P., Kisielewska, D. *et al.* Feasibility study of the positronium imaging with the J-PET tomograph. *arXiv:1805.11696, Submitted to: Phys. Med. Biol.* (2018).

28. Alavi-Harati, A. *et al.* A Measurement of the K(L) charge asymmetry. *Phys. Rev. Lett.* **88,** 181601–181606 (2002).

29. Archibald, W. J. Polyelectrons. *Annals of the New York Academy of Sciences* **48,** 219–238 (1946).

30. Ore, A. & Powell, J. L. Three-Photon Annihilation of an Electron-Positron Pair. *Phys. Rev.* **75,** 1696–1699 (1949).

31. Gninenko, S. N., Krasnikov, N. V., Matveev, V. A. & Rubbia, A. Some aspects of positronium physics. *Physics of Particles and Nuclei* **37,** 321–346 (2006).

32. Conti, R., Hatamian, S., Lapidus, L., Rich, A. & Skalsey, M. Search for C-violating, P-conserving interactions and observation of 23S1 to 21P1 transitions in positronium. *Phys. Lett. A* **177,** 43–48 (1993).

33. Arbic, B. K., Hatamian, S., Skalsey, M., Van House, J. & Zheng, W. Angular-correlation test of CPT in polarized positronium. *Phys. Rev. A* **37,** 3189–3194 (1988).

34. Lee-Franzini, J. & Franzini, P. A Flavor of KLOE. *Acta Phys. Polon.* **B38,** 2703–2730 (2007).

35. *The DAFNE injection system and layout* `www.lnf.infn.it/acceleratori/dafne/injection.html`. Accessed: 2017-12-06.

36. Patrignani, C. *et al.* Review of Particle Physics. *Chinese Physics* **C40,** 100001 (2016).

37. Aloisio, A. *et al. Studies of Ko(S) decays with the KLOE detector at DAPHNE* in *Lepton and photon interactions at high energies. Proceedings, 20th International Symposium, LP 2001, Rome, Italy, July 23-28, 2001* (2001).

38. Aloiso, A. *et al.* The KLOE drift chamber. *Nucl. Instrum. Meth. A* **494,** 163–172 (2002).

39. Sciascia, B. *Studies of charged kaon decays with the KLOE experiment* PhD thesis (University La Sapienza (Rome), 2000).

40. Adinolfi, M. *et al.* The KLOE electromagnetic calorimeter. *Nucl. Instrum. Meth. A* **482,** 364 (2002).

41. Adinolfi, M. *et al.* The trigger system of the KLOE experiment. *Nucl. Instrum. Meth. A* **492,** 134–146 (2002).

42. Bloise, C. & Incagli, M. *The Event Classification module and the ECLO, ECLS banks* KLOE Memo 175. 1999.

43. Bloise, C. & Incagli, M. *The Event Classification procedures* KLOE Memo 225. 2000.

44. Moulson, M. & Muller, S. *FILFO revisited: A new look at the offline reconstruction filter and event classification* KLOE Memo 288. 2004.

45. Ambrosino, F. *et al.* Data handling, reconstruction, and simulation for the KLOE experiment. *Nucl. Instrum. Meth. A* **534,** 403–433 (2004).

46. Krzemien, W. A new event display for the KLOE-2 experiment. *Acta Phys. Polon.* **B46,** 95–99 (2015).

47. Silarski, M. *Search for the CP symmetry violation in the decays of K_S mesons using the KLOE detector* PhD thesis (Jagiellonian University (Krakow), 2012).

48. Babusci, D. *et al.* A new limit on the CP violating decay $K_S \to 3\pi^0$ with the KLOE experiment. *Phys. Lett. B* **723,** 54–60 (2013).

49. Cabibbo, G. & Spadaro, T. *K_{crash} tag realted studies* KLOE Memo 210. 2000.

50. De Lucia, E. *Measurement of the branching ratio of the $K^+ \to \pi^+\pi^0(\gamma)$ decay* KLOE Memo 340. 2007.

51. CERN Information Technology Division. *HBOOK Statistical Analysis and Histogramming* Reference Manual. 1998.

52. Barlow, R. & Beeston, C. Fitting using finite Monte Carlo samples. *Comput. Phys. Commun.* **77,** 219–228 (1993).

53. Barker, S. & Cousin, R. D. Clarification of the use of chi-square and likelihood function in fits to histogram. *Nucl. Inst. Meth. A* **221,** 437–442 (1983).

54. Ambrosino, F. *et al.* Determination of CP and CPT violation parameters in the neutral kaon system using the Bell-Steinberger relation and data from the KLOE experiment. *JHEP* **12,** 011 (2006).

55. Amelino-Camelia, G. *et al.* Physics with the KLOE-2 experiment at the upgraded DAΦNE. *Eur. Phys. J.* **C68,** 619–681 (2010).

56. Zobov, M. *et al.* Test of "Crab-Waist" Collisions at the DAΦNE Φ Factory. *Phys. Rev. Lett.* **104,** 174801–174806 (2010).

57. Milardi, C. *et al.* High luminosity interaction region design for collisions inside high field detector solenoid. *Journal of Instrumentation* **7,** T03002 (2012).

58. Pałka, M., ..., Kamińska, D., *et al.* Multichannel FPGA based MVT system for high precision time (20 ps RMS) and charge measurement. *JINST* **12,** P08001 (2017).

59. Korcyl, G., ..., Kamińska, D., *et al.* Sampling FEE and Trigger-less DAQ for the J-PET Scanner. *Acta Phys. Polon. B* **47,** 491–497 (2016).

60. Moskal, P. *Patent* US 8859973B2 (2014), PL 388555 (2009).

61. Vandenberghe, S., Mikhaylova, E., D'Hoe, E., Mollet, P. & Karp, J. S. Recent developments in time-of-flight PET. *EJNMMI Physics* **3,** 3 (2016).

62. Gupta Sharma, N. *Hit-time and hit-position reconstruction of gamma quanta in the J-PET tomography system based on a library of model signals* PhD thesis (Jagiellonian University, 2017).

63. Smyrski, J., ..., Kamińska, D., *et al.* Measurement of gamma quantum interaction point in plastic scintillator with WLS strips. *Nucl. Instrum. Meth. A* **851,** 39–42 (2017).

64. Raczyński, L. *et al.* Novel method for hit-position reconstruction using voltage signals in plastic scintillators and its application to Positron Emission Tomography. *Nucl. Instrum. Meth. A* **764,** 186–192 (2014).

65. Raczyński, L., ..., Kamińska, D., *et al.* Compressive Sensing of Signals Generated in Plastic Scintillators in a Novel J-PET Instrument. *Nucl. Instrum. Meth. A* **786,** 105–112 (2015).

66. Raczyński, L, ..., Kamińska, D., *et al.* Calculation of the time resolution of the J-PET tomograph using kernel density estimation. *Phys. in Med. and Biol.* **62,** 5076–5097 (2017).

67. Moskal, P., ..., Kamińska, D., *et al.* Potential of the J-PET detector for studies of discrete symmetries in decays of positronium atom - a purely leptonic system. *Acta Phys. Polon. B* **47,** 509–537 (2016).

68. Moskal, P., ..., Kamińska, D., *et al.* A novel method for the line-of-response and time-of-flight reconstruction in TOF-PET detectors based on a library of synchronized model signals. *Nucl. Instrum. Meth. A* **775,** 54–62 (2015).

69. Pawlik-Niedźwiecka, M., ..., Kisielewska, D., *et al.* Preliminary Studies of J-PET Detector Spatial Resolution. *Acta Phys. Pol. A* **132,** 1645–1648 (2017).

70. Klein, O. & Nishina, Y. Über die Streuung von Strahlung durch freie Elektronen nach der neuen relativistischen Quantendynamik von Dirac. *Zeitschrift für Physik* **52,** 853–868 (1929).

71. Jin-Jie, W. *et al.* A study of time over threshold (TOT) technique for plastic scintillator counter. *Chin. Phys. C* **32,** 186 (2008).

72. Moskal, P. *et al.* Test of a single module of the J-PET scanner based on plastic scintillators. *Nucl. Instrum. Meth. A* **764,** 317–321 (2014).

73. Bettinardi, V. *et al.* Physical Performance of the new hybrid PET/CT Discovery-690. *Medical Physics* **38,** 5394–5411 (2011).

74. Surti, S. *et al.* Performance of Philips Gemini TF PET/CT Scanner with Special Consideration for Its Time-of-Flight Imaging Capabilities. *Journal of Nuclear Medicine* **48,** 471–480 (2007).

75. Krzemień, W. *et al.* Analysis framework for the J-PET scanner. *Acta Phys. Polon. A* **127,** 1491–1494 (2015).

76. Rene Brun and Fons Rademaker. ROOT - An Object Oriented Data Analysis Framework. *Nucl. Instrum. Meth. A* **389,** 81–86 (1997).

77. J-PET Collaboration. *J-PET Analysis Framework* github.com/JPETTomography/j-pet-framework.git. 2018.

78. Agostinelli, S. *et al.* GEANT4: A Simulation toolkit. *Nucl. Instrum. Meth. A* **506,** 250–303 (2003).

79. J-PET Collaboration. *J-PET-geant4* github.com/JPETTomography/J-PET-geant4.git. 2018.

80. Y. C. Jean, P. E. M. & Schrader, D. M. *Positron and Positronium Chemistry* (World Scientific Publishing, 2003).

81. Colombino, P. & Fiscella, B. Positronium annihilation in magnetic fields up to 21 kG. *Il Nuovo Cimento B (1971-1996)* **3,** 1 (2008).

82. Jasińska, B. & Moskal, P. A new PET diagnostic indicator based on the ratio of 3gamma/2gamma positron annihilation. *Acta Phys. Polon. B* **48,** 1577 (2017).

83. Jasińska, B., ..., Kamińska, D., *et al.* Determination of the 3γ fraction from positron annihilation in mesoporous materials for symmetry violation experiment with J-PET scanner. *Acta Phys. Polon. B* **47,** 453–461 (2016).

84. *Organic Scintillation Materials* http://www.crystals.saint-gobain.com/uploadedFiles/SG-Crystals/Documents/SGC%20Organics%20Brochure.pdf. Accessed: 10.02.2016. 2013.

85. Conti, M. State of the art and challenges of time-of-flight PET. *Phys. Med.* **25,** 1–11 (2009).

86. Strzelecki, A. *Image reconstruction and simulation of strip Positron Emission Tomography scanner using computational accelerators* PhD thesis (Jagiellonian University, 2016).

87. Berestetskii, V., Lifshitz, E. & Pitaevsk, L. *Relativistic Quantum Theory* (Pergamon Pres, Headington Hill Hal, Oxford, 1971).

88. Baxter, A. *et al.* Compton-suppression tests on Ge and BGO prototype detectors for GAMMASPHERE. *Nucl. Instrum. Meth. A* **317,** 101–110 (1992).

89. Gajos, A., Kamińska, D, *et al.* Trilateration-based reconstruction of ortho-positronium decays into three photons with the J-PET detector. *Nucl. Instrum. Meth. A* **819,** 54–59 (2016).

90. Gajos, A. *Investigations of fundamental symmetries with the electron-positron systems* PhD thesis (Jagiellonian University, 2018).

91. Mills, A. P. & Berko, S. Search for C Nonconservation in Electron-Positron Annihilation. *Phys. Rev. Lett.* **18,** 420–425 (1967).

92. G. Morello et al. The cylindrical GEM detector for the KLOE-2 Inner Tracker. *JINST* **9** (2013).

93. Bernabeu, J., Di Domenico, A. & Villanueva-Perez, P. Probing CPT in transitions with entangled neutral kaons. *JHEP* **2015,** 139–159 (2015).

94. Engelhardt, N., Nelson, A. E. & Walsh, J. R. Apparent CPT violation in neutrino oscillation experiments. *Phys. Rev. D* **81,** 113001–113009 (2010).

95. Myers, E. G. CPT tests with the antihydrogen molecular ion. *Phys. Rev. A* **98,** 010101–010107 (2018).